Tracing the substrate translocation mechanism in P-glycoprotein

Theresa Gewering[1,2]†, Deepali Waghray[3]†, Kristian Parey[1,2,4], Hendrik Jung[5], Nghi N.B. Tran[6], Joel Zapata[6], Pengyi Zhao[7], Hao Chen[7], Dovile Januliene[1,2,4], Gerhard Hummer[5,8], Ina L. Urbatsch[6], Arne Moeller[1,2,4]*‡, Qinghai Zhang[3]*‡

[1]Osnabrück University, Department of Biology/Chemistry, Structural Biology section, 49076 Osnabrück, Germany.

[2]Department of Structural Biology, Max Planck Institute of Biophysics, 60438 Frankfurt am Main, Germany.

[3]Department of Integrative Structural and Computational Biology, The Scripps Research Institute, La Jolla, CA 92037, USA.

[4]Osnabrück University, Center of Cellular Nanoanalytic Osnabrück (CellNanOs), 49076 Osnabrück, Germany

[5]Department of Theoretical Biophysics, Max Planck Institute of Biophysics, 60438 Frankfurt am Main, Germany.

[6]Department of Cell Biology and Biochemistry, Texas Tech University Health Sciences Center, Lubbock, TX 79430, USA.

[7]Department of Chemistry & Environmental Science, New Jersey Institute of Technology, Newark, New Jersey 07102, USA.

[8]Institute for Biophysics, Goethe University Frankfurt, 60438 Frankfurt am Main, Germany.

*Corresponding author. Email: arne.moeller@uos.de (A.M.); qinghai@scripps.edu (Q.Z.)

† These authors contributed equally to this work.

‡These authors contributed equally to this work.

Abstract

P-glycoprotein (Pgp) is a prototypical ABC transporter of great biological and clinical significance that confers cancer multidrug resistance and mediates the bioavailability and pharmacokinetics of many drugs[1-3]. Decades of structural and biochemical studies have provided insights into how Pgp binds diverse compounds[4-9], but how they are translocated through the membrane has remained elusive. Here, we covalently attached a cyclic substrate to discrete sites of Pgp and determined multiple complex structures in inward- and outward-facing states by cryoEM. In conjunction with molecular dynamics simulations, our structures trace the substrate passage across the membrane and identify conformational changes in transmembrane helix 1 (TM1) as regulators of substrate transport. In mid-transport conformations, TM1 breaks at glycine 72. Mutation of this residue significantly impairs drug transport of Pgp in vivo, corroborating the importance of its regulatory role. Importantly, our data suggest that the cyclic substrate can exit Pgp without the requirement of a wide-open outward-facing conformation, diverting from the common efflux model for Pgp and other ABC exporters. The substrate transport mechanism of Pgp revealed here pinpoints critical targets for future drug discovery studies of this medically relevant system.

Main Text:

P-glycoprotein (Pgp, also known as MDR-1 and ABCB1) is a prominent member of the human ATP-binding cassette (ABC) efflux transporters that removes a large variety of chemically unrelated hydrophobic compounds from cells[3,9]. Pgp is highly expressed in the liver, kidney, and intestines, where it limits absorption and enhances the excretion of cytotoxic compounds[10-12]. In the blood-brain, blood-testis, and blood-placenta barriers, Pgp protects and detoxifies those sanctuaries from xenobiotics[13-15]. Of central importance for many chemotherapeutic treatments, Pgp is a major determinant of drug bioavailability and pharmacokinetics and confers multidrug resistance in several diseases, most notably cancer[16-18]. Consequently, evasion, selective inhibition, and modulation of Pgp transport are important goals in drug development, but are hindered by a lack of detailed understanding of the drug transport mechanisms[19].

For Pgp and ABC transporters in general, ATP binding, hydrolysis, and subsequent release of the cleaved products (inorganic phosphate and ADP) fuel large-scale conformational changes that ultimately result in translocation of substrates across the membrane bilayer[20,21]. In inward-facing (IF) conformations, the nucleotide-binding domains (NBDs) are separated, and substrates can access a large binding cavity that is open to the lower membrane leaflet and cytoplasm. ATP-induced dimerization of the NBDs promotes large rearrangements of the transmembrane domains (TMDs) from an IF to an outward-facing (OF) conformation, from which the substrate is released[22,23]. Pgp structures with bound substrates and inhibitors in IF conformations have revealed one or more overlapping binding sites[6-8,24,25]. Multimodal binding mechanisms for chemically related compounds have been proposed[6,9], including access of hydrophobic ligands from the lipid-protein interface to the binding sites of Pgp[8,24]. However, structural data that elucidate how substrates are shuttled across the lipid bilayer to the extracellular space are unavailable at present.

So far, only a single OF structure of mammalian Pgp has been described, but without detectable substrate density[26]. Most insights into the transport pathway arise from molecular dynamics simulations, which are also limited by the scarcity of available structural details[27,28]. Consequently, the molecular mechanics that move the substrate through the transmembrane passage have remained elusive. To address this fundamental question and overcome the dynamic and transient nature of substrate translocation, we tethered a substrate molecule covalently to specific residues along the putative translocation pathway of Pgp and utilized cryoEM to capture Pgp structures with bound substrate during various stages of transport.

Covalent ligand design for Pgp labeling

For covalent labeling of Pgp, we synthesized a derivative of the previously published QZ-Ala tripeptide substrate[24], by substituting one of the three Ala with Cys that is disulfide-linked to a 2,4-dinitrophenyl thiolate group (designated AAC-DNPT, See **Methods**, Extended Data Fig. 1). QZ-Ala is a strong ATPase stimulator and subject to Pgp transport as evidenced by its reduced cytotoxicity in cells overexpressing Pgp[24]. Additionally, we have measured Pgp-mediated transport of QZ-Ala in the MDCK-MDR1 monolayer permeability assay (see **Methods**). The efflux ratio (R_E) of QZ-Ala was determined as 2.5. In the presence of the Pgp inhibitor cyclosporin A, R_E was 0.9, indicating that the Pgp-specific transport of QZ-Ala was inhibited. Derivatizing QZ-Ala is simplified by its structural symmetry, which reduces the complexity of modifying this transport substrate for attaching to Pgp in different states. Furthermore, attachment of DNPT strongly activates disulfide exchange, allowing rapid and efficient crosslinking between the cyclic peptide and accessible cysteines. Free DNPT, released during crosslinking, is bright yellow. This provides a simple, visible readout that can be monitored with a UV-Vis spectrometer (Fig. 1a). Four single-Cys mutants of Pgp (Pgp335, Pgp978, Pgp971, and Pgp302) were generated for

crosslinking, and mutations were chosen near the two previously reported QZ-Ala binding sites[24]. L335C in transmembrane helix 6 (TM6) and V978C in TM12 are situated at symmetric positions on opposing TMD halves, while L971C is located two helical turns above V978 (Fig. 1b). Residues L335C, V978C as well as I302C located in TM5 were previously shown to be labeled with verapamil[29]. Based on the appearance of the yellow DNPT byproduct, Pgp335 and Pgp978 reacted with AAC-DNPT within minutes, while Pgp971 and Pgp302 did not. Even after extended incubations only background absorbances were detected comparably to Cys-less Pgp (CL-Pgp) (Fig. 1c). Only after adding Mg^{2+}ATP to fuel substrate translocation, Pgp971 could react with AAC-DNPT, but Pgp302 could not. Covalent attachment of the cyclic peptide AAC was further validated by high-resolution mass spectrometry of trypsin-digested peptide fragments (Extended Data Figs. 2 to 4). The presence of noncovalent transport substrates such as QZ-Ala or verapamil increase ATP hydrolysis in CL-Pgp and the single Cys mutants (Extended Data Fig. 5a). Similar to QZ-Ala, AAC-DNTP stimulated ATPase activity of CL-Pgp at low concentrations; with half-maximal enhancement of activity (EC50) seen at submicromolar concentrations, suggesting that it also acts as substrate (Extended Data Fig. 5b). At higher concentrations, the rate of ATP hydrolysis is significantly reduced in the mutants compared to CL-Pgp indicative of cross-linking AAC-DNPT with the single Cys mutants (Fig. 1d and Extended Data Fig. 5b). Importantly, Pgp335 and Pgp978 retain notably higher ATPase activity after cross-linking than the respective apo-Pgp mutants in the absence of substrate (Extended Data Fig. 5b and Fig. 1d), suggesting that tethered AAC still acts as a substrate and that Pgp335 and Pgp978 cycle between IF and OF conformations.

Pgp structures with bound substrates

To capture different conformations during the transport cycle of Pgp, we mutated the catalytic glutamate residues in the Walker-B motifs of each NBD (E552Q/E1197Q) in Pgp335 and Pgp978.

When Mg^{2+}ATP is present, these mutations arrest the enzyme in an ATP-occluded, NBD-dimerized conformation that resembles the pre-hydrolysis state[26]. For Pgp971, we prepared the covalent complex in the presence of Mg^{2+} ATP and stabilized the resulting OF complex with vanadate in a post-hydrolysis intermediate state[30,31] (Fig. 1c). CryoEM analysis of the respective covalent complexes in both OF and IF conformations provided eight high-resolution structures with zero, one, or two ligands bound. In addition, a control dataset with ATP, but without the substrate was collected for Pgp335 (Fig. 2, Extended Data Fig. 6 and 7, and Extended Data Table 1).

The IF-structure of Pgp335, solved at 3.8 Å resolution, shows clear densities for two substrate molecules: one crosslinked and one not (IF335-2lig, Fig. 2 and Extended Data Fig. 7 and 8). The non-crosslinked molecule is bound in a position that resembles the one previously reported in a crystal structure[24]. It interacts closely with the covalently-linked substrate, which is situated further up the membrane. Both ligand molecules are oriented along the vertical axis of the protein and positioned side-by-side through hydrophobic interactions. The uncleaved DNPT group of the non-crosslinked substrate is evident in the cryoEM density map. Two substrate molecules are also bound in the IF structure of Pgp978 (IF978-2lig); the non-covalently bound molecule is clearly visible at a similar position as in IF335-2lig, while the crosslinked substrate is located on the opposite side of the binding cavity near TM12 (Extended Data Fig. 8). Corroborating our labeling data (Fig. 1c), in the IF structure of Pgp971 (IF971-1lig) at 4.3 Å resolution, only the non-crosslinked substrate is bound at the approximate location seen for non-crosslinked substrate in IF335-2lig and IF978-2lig (Fig. 2 , Extended Data Figs. 8 and 9e).

Multi-model cryoEM analyses of ATP-bound Pgp335 revealed three different OF conformations within a single dataset: ligand-free (42%), single-ligand-bound (34%), and double-ligand-bound (26%) (OF335-nolig, OF335-1lig and OF335-2lig), at 2.6 Å, 2.6 Å, and 3.1 Å resolution, respectively (Extended Data Fig. 10, Fig. 2). For Pgp978 and Pgp971, only OF conformations with a single bound ligand (OF978-1lig and OF971-1lig, Fig. 2) were detected at 2.9 Å and 3 Å resolution, respectively.

Substrate translocation pathway

In the OF structures with a single bound substrate, the central transmembrane helices TM1, TM6, TM7 and TM12 bulge outwards to accommodate the substrate in a small tunnel (Extended Data Fig. 11). Comparing the ligand positions between the IF and OF structures, in IF335-2lig to OF335-1lig, and IF978-2lig to OF978-1lig, the covalently attached ligand pivots around the respective Cys residue by almost 180°, moving it further up the translocation tunnel (Extended Data Figs. 8 and 9a,b, and Supplementary Videos 1 and 2). Our data do not reveal whether rotation of the ligand during the IF-OF conformational change is required for transport or if this reflects the fact that the ligand is covalently pinned to the crosslinking residue. However, the observation of ligand rotation illustrates how much space is available in the binding cavity during this conformational transition. The ligand position and orientation in OF335-1lig and OF978-1lig overall coincide well, with the latter shifting up slightly (Extended Data Fig. 9d). This finding indicates that the export tunnel is inherent to substrate translocation regardless of the initial binding position in the IF conformation. As such, our data suggest a single common pathway for substrate export in Pgp, contrary to the dual pseudosymmetric pathways suggested earlier[28,32].

OF971-1lig captures a later-stage transport intermediate, in which the compound resides approximately 7 Å further up the translocation tunnel and is coordinated by highly conserved residues, including M74 and F78 (Figs. 2 and 3b, Extended Data Figs. 8 and 12). As no crosslinked substrate was detected in the corresponding IF structure, the substrate was likely transported to residue L971C before the crosslinking reaction could take place. Substrate entry from the extracellular side is less likely given the small opening of the substrate translocation pathway in all OF Pgp structures with or without bound substrate obtained here and previously[26]. In all substrate bound OF conformations methionines and phenylalanines at different positions seem to be important for ligand coordination in all of the Pgp structures (Extended Data Fig. 12). As expected, the substrate is held in the binding pocket mainly by the hydrophobic interactions throughout the different conformations (Extended Data Figs. 8 and 12). In the OF335-nolig structure, as well as in the virtually indistinguishable control, the translocation tunnel is collapsed, which shields the substrate binding pocket from the extracellular milieu and prevents re-entry from this side[26].

Regulatory role of TM1

The series of IF and OF Pgp structures reveal a cascade of conformational changes in TM1, which displays significant plasticity throughout the different transport stages (Fig. 2, Extended Data Fig. 8, and Supplementary Videos 1, 2 and 3). In IF conformations, TM1 is a long, straight helix (Fig. 2 and Extended Data Fig. 8). However, in OF335-1lig, OF978-1lig, and OF971-1lig, TM1 swings out at A63, dilating the transmembrane passage and providing sufficient space for accommodating the bound ligand. At the same time, a pronounced kink at G72 on TM1 destabilizes the helix and the extracellular loop of Pgp between TM1 and TM2 and leads to a partial unwinding. This conformational deformation shields the intramembranous tunnel from the extracellular

environment, with TM1 acting as a lid, almost parallel to the membrane (Fig. 2 and 4a, Extended Data Fig. 8). Strikingly, along with the upward movement of the ligand (from L335C to V978C to L971C), the TM1 loop is progressively lifted and restabilized. Ultimately, as shown previously[26] and by our OF335-nolig structure, the helix is straightened upon the release of the ligand (Fig. 4a, Extended Data Fig. 8). Interestingly, the extracellular gate is sealed in all OF structures, which is especially surprising for OF971-1lig where the ligand is near the tunnel exit (Fig. Extended Data Fig. 11).

Using OF978-1lig as initial configuration, we performed molecular dynamics (MD) simulations of Pgp embedded in a lipid bilayer to validate the proposed substrate escape pathway. Accelerated by temperature (T=400 K), we observed movement and release of the non-covalently bound substrate to the extracellular side moderated by interactions between the ligand and hydrophobic residues in the upper part of TM1 (Supplementary Video 3). The intermediate steps coincided well with the conformations observed in cryoEM (Fig. 4, Extended Data Figs. 13 and 14). Without any bias imposed, the substrate progressed to a position closely matching OF971-1lig (Fig. 2, 4b). Then, while TM1 gradually refolded from the intracellular side, the substrate wiggled out to form transient interactions with the still unstructured extracellular part of TM1 (Fig. 4). Importantly, the substrate escaped without Pgp experiencing a wide opening of the extracellular region. After the substrate left the exit tunnel, TM1 continued to refold to attain a straight helix configuration like OF335-nolig at the end of the simulation (Fig. 4). Overall, with exception of TM1, motions in Pgp to accommodate the moving substrate were mostly limited to small dilations of the transmembrane helices, supporting our observations from cryoEM.

Our cryoEM structures and MD simulations revealed an important regulatory role of TM1 during substrate transport, emphasizing the helix-breaking G72. Therefore, we mutated this residue, which is highly conserved in mammalian Pgp (Fig. 3), to a helix-stabilizing alanine[33] and tested the mutant's ability to export structurally diverse fungicides and to convey drug resistance *in vivo*. Compared to the wild-type and CL-Pgp, the G72A mutant expressed normally in *Saccharomyces cerevisiae* (Fig. 3c), but showed significantly reduced growth resistance to the test drugs including doxorubicin, FK506, and valinomycin (Fig. 3d). As drug transport was severely impaired, we further investigated the mutant's ATPase activity. In presence of transport substrates such as FK506, valinomycin, or verapamil the ATPase activity of WT Pgp was significantly stimulated; however, the G72A mutant displayed only low levels of basal ATPase activity (in the absence of drug) and the response to drug stimulation was greatly diminished over a range of concentrations tested (Fig. 3e-g). To reveal potential structural consequences responsible for the loss of function, we performed cryoEM on the Pgp335 G72A mutant after crosslinking the single cysteine L335C with AAC-DNTP and stabilizing the OF complex with Mg^{2+} ATP and vanadate in a post-hydrolysis intermediate state. After multi-model classification, two conformations emerged. The first conformation, resolved at 3.0 Å, shows no substrate bound in analogy to OF335-nolig. The second dominant conformation is, however, much more heterogenous, resulting in a reduced and anisotropic resolution of approximately 4.6 Å (Extended Data Fig. 15). Here, the NBDs are well resolved but several transmembrane helices are missing, including TM1 in which residue G72A is located. The structural disorder, observed in the transmembrane region, is likely a result of the tethered ligand, causing local distortion of the surrounding α-helices as TM1 may not be able to kink at G72 in the mutant, which could explain its impaired transport function. Collectively, the significant differences in drug resistance profiles and drug-stimulated ATP hydrolysis rates

between the G72A mutant and WT-Pgp along with our structural findings substantiate and highlight the key role of TM1 for the regulation of substrate transport in Pgp.

Discussion

Our data suggest a mechanism for how Pgp mediates substrate transport. Transport commences in the IF conformation with binding of the substrate. Upon ATP-induced NBD-dimerization, the transporter converges into an OF conformation in which the intracellular gate is closed. The presence of the substrate in the OF conformation of Pgp dislocates TM1 at A63 and introduces a sharp kink at G72, forcing the helix to unwind partially between TM1 and TM2 (Fig. 4 and Extended Data Fig. 8). This enlarges the extracellular loop which shields the transmembrane tunnel from the extracellular environment and guides the substrate to move up the translocation tunnel, allowing TM1 to gradually restabilize. During the last stages of transport (OF971-1lig to OF335-nolig), the TM1-TM2 regulatory loop straightens, and the substrate-interacting hydrophobic residues (M74 and F78) rotate and pivot away from the tunnel, which facilitates the escape of the substrate from the transporter. Although OF971-1lig captured a post-hydrolysis state, we cannot rule out the possibility of ligand release prior to ATP hydrolysis, when it is not covalently bound. Notwithstanding, the proposed TM1 kinking and straightening mechanism of substrate expulsion would obviate the requirement for the Y-shaped, wide-open OF conformation reported for multiple bacterial ABC transporters[34,35], suggesting a substrate-dependent transport mechanism in Pgp, or else a divergence of mechanisms among ABC transporters.

For the OF335-2lig structure, observed in the same data set as OF335-1lig and OF335-nolig, we hypothesize that the hydrophobic nature of the substrate promotes the binding of two substrate molecules to each other. MD simulations with this structure as a starting conformation reveal no

separation of the two molecules, suggesting that they might be treated as one bigger substrate in the transport event. With the binding positions differing between OF335-1lig and OF335-2lig (Extended Data Fig. 9c, 12 and 16), neither the cryoEM structure nor the simulations allow conclusions about a possible transport mechanism of two ligands at this point.

How ABC transporters move substrates through the lipid bilayer has been a long-standing question[36]. The scarcity of high-resolution structures of substrate-bound OF conformations[37], especially in the highly transient intermediate states, has severely limited our understanding of this vital process. Here, we were able to determine eight high-resolution structures of the archetypical ABC transporter Pgp, revealing the underlying molecular mechanics of substrate translocation. In general, the large number and diversity of ABC transporters, and the even wider variety of their substrates, make it unlikely that a universal substrate translocation mechanism will emerge. Our strategy of stalling the otherwise highly transient intermediates in this process through crosslinking and subsequent high-resolution cryoEM analysis could serve as a blueprint to understand the transport mechanisms of lipid transporters as well as other members of the transporter family.

Main References

1 Juliano, R. L. & Ling, V. A surface glycoprotein modulating drug permeability in Chinese hamster ovary cell mutants. *Biochim. Biophys. Acta* **455**, 152-162, doi:10.1016/0005-2736(76)90160-7 (1976).

2 Ueda, K. *et al.* The mdr1 gene, responsible for multidrug-resistance, codes for P-glycoprotein. *Biochem. Biophys. Res. Commun.* **141**, 956-962, doi:10.1016/s0006-291x(86)80136-x (1986).

3 Sharom, F. J. The P-glycoprotein multidrug transporter. *Essays Biochem.* **50**, 161-178, doi:10.1042/bse0500161 (2011).

4 Loo, T. W. & Clarke, D. M. Identification of residues within the drug-binding domain of the human multidrug resistance P-glycoprotein by cysteine-scanning mutagenesis and reaction with dibromobimane. *J. Biol. Chem.* **275**, 39272-39278, doi:10.1074/jbc.M007741200 (2000).

5 Loo, T. W., Bartlett, M. C. & Clarke, D. M. Identification of residues in the drug translocation pathway of the human multidrug resistance P-glycoprotein by arginine mutagenesis. *J. Biol. Chem.* **284**, 24074-24087, doi:10.1074/jbc.M109.023267 (2009).

6 Aller, S. G. *et al.* Structure of P-glycoprotein reveals a molecular basis for poly-specific drug binding. *Science* **323**, 1718-1722, doi:323/5922/1718 [pii] 10.1126/science.1168750 (2009).

7 Alam, A., Kowal, J., Broude, E., Roninson, I. & Locher, K. P. Structural insight into substrate and inhibitor discrimination by human P-glycoprotein. *Science* **363**, 753-756, doi:10.1126/science.aav7102 (2019).

8 Nosol, K. *et al.* CryoEM structures reveal distinct mechanisms of inhibition of the human multidrug transporter ABCB1. *Proc. Natl. Acad. Sci. U. S. A.* **117**, 26245-26253, doi:10.1073/pnas.2010264117 (2020).

9 Chufan, E. E., Sim, H. M. & Ambudkar, S. V. Molecular basis of the polyspecificity of P-glycoprotein (ABCB1): recent biochemical and structural studies. *Adv. Cancer Res.* **125**, 71-96, doi:10.1016/bs.acr.2014.10.003 (2015).

10 Thiebaut, F. *et al.* Cellular localization of the multidrug-resistance gene product P-glycoprotein in normal human tissues. *Proc. Natl. Acad. Sci. U. S. A.* **84**, 7735-7738, doi:10.1073/pnas.84.21.7735 (1987).

11 Cascorbi, I. P-glycoprotein: tissue distribution, substrates, and functional consequences of genetic variations. *Handb. Exp. Pharmacol*. 261-283, doi:10.1007/978-3-642-14541-4_6 (2011).

12 Cordon-Cardo, C. *et al.* Expression of the multidrug resistance gene product (P-glycoprotein) in human normal and tumor tissues. *J. Histochem. Cytochem.* **38**, 1277-1287, doi:10.1177/38.9.1974900 (1990).

13 Schinkel, A. H. P-Glycoprotein, a gatekeeper in the blood-brain barrier. *Adv. Drug Deliv. Rev.* **36**, 179-194 (1999).

14 Borst, P. & Schinkel, A. H. P-glycoprotein ABCB1: a major player in drug handling by mammals. *J. Clin. Invest.* **123**, 4131-4133, doi:10.1172/JCI70430 (2013).

15 Fromm, M. F. Importance of P-glycoprotein at blood-tissue barriers. *Trends Pharmacol. Sci.* **25**, 423-429, doi:10.1016/j.tips.2004.06.002 (2004).

16 Szakacs, G., Paterson, J. K., Ludwig, J. A., Booth-Genthe, C. & Gottesman, M. M. Targeting multidrug resistance in cancer. *Nature reviews. Drug Discov.* **5**, 219-234, doi:nrd1984 [pii] 10.1038/nrd1984 (2006).

17 Gottesman, M. M. & Ling, V. The molecular basis of multidrug resistance in cancer: the early years of P-glycoprotein research. *FEBS Lett.* **580**, 998-1009, doi:S0014-5793(05)01543-7 [pii] 10.1016/j.febslet.2005.12.060 (2006).
18 Giacomini, K. M. *et al.* Membrane transporters in drug development. *Nat. Rev. Drug Discov.* **9**, 215-236, doi:10.1038/nrd3028 (2010).
19 Waghray, D. & Zhang, Q. Inhibit or Evade Multidrug Resistance P-Glycoprotein in Cancer Treatment. *J. Med. Chem.* **61**, 5108-5121, doi:10.1021/acs.jmedchem.7b01457 (2018).
20 Rees, D. C., Johnson, E. & Lewinson, O. ABC transporters: the power to change. *Nature reviews. Mol. Cell Biol.* **10**, 218-227, doi:10.1038/nrm2646 (2009).
21 Hofmann, S. *et al.* Conformation space of a heterodimeric ABC exporter under turnover conditions. *Nature* **571**, 580-583, doi:10.1038/s41586-019-1391-0 (2019).
22 Januliene, D. & Moeller, A. CryoEM of ABC transporters: an ice-cold solution to everything? *FEBS Lett.* **594**, 3776-3789, doi:10.1002/1873-3468.13989 (2020).
23 Verhalen, B. *et al.* Energy transduction and alternating access of the mammalian ABC transporter P-glycoprotein. *Nature* **543**, 738-741, doi:10.1038/nature21414 (2017).
24 Szewczyk, P. *et al.* Snapshots of ligand entry, malleable binding and induced helical movement in P-glycoprotein. *Acta Crystallogr. Section D: Biol. Crystallogr.* **71**, 732-741, doi:10.1107/S1399004715000978 (2015).
25 Alam, A. *et al.* Structure of a zosuquidar and UIC2-bound human-mouse chimeric ABCB1. *Proc. Natl. Acad. Sci. U. S. A.* **115**, E1973-E1982, doi:10.1073/pnas.1717044115 (2018).
26 Kim, Y. & Chen, J. Molecular structure of human P-glycoprotein in the ATP-bound, outward-facing conformation. *Science* **359**, 915-919, doi:10.1126/science.aar7389 (2018).
27 Goddeke, H. & Schafer, L. V. Capturing substrate translocation in an ABC exporter at the atomic level. *J. Am. Chem. Soc.* **142**, 12791-12801, doi:10.1021/jacs.0c05502 (2020).
28 McCormick, J. W., Vogel, P. D. & Wise, J. G. Multiple drug transport pathways through human P-Glycoprotein. *Biochemistry* **54**, 4374-4390, doi:10.1021/acs.biochem.5b00018 (2015).
29 Loo, T. W. & Clarke, D. M. Defining the drug-binding site in the human multidrug resistance P-glycoprotein using a methanethiosulfonate analog of verapamil, MTS-verapamil. *J. Biol. Chem.* **276**, 14972-14979, doi:10.1074/jbc.M100407200 (2001).
30 Urbatsch, I. L., Sankaran, B., Bhagat, S. & Senior, A. E. Both P-glycoprotein nucleotide-binding sites are catalytically active. *J. Biol. Chem.* **270**, 26956-26961, doi:10.1074/jbc.270.45.26956 (1995).
31 Moeller, A. *et al.* Distinct Conformational spectrum of homologous multidrug ABC transporters. *Structure* **23**, 450-460, doi:10.1016/j.str.2014.12.013 (2015).
32 Parveen, Z. *et al.* Molecular dissection of dual pseudosymmetric solute translocation pathways in human P-glycoprotein. *Mol. Pharmacol.* **79**, 443-452, doi:10.1124/mol.110.067611 (2011).
33 Lopez-Llano, J., Campos, L. A. & Sancho, J. Alpha-helix stabilization by alanine relative to glycine: roles of polar and apolar solvent exposures and of backbone entropy. *Proteins* **64**, 769-778, doi:10.1002/prot.21041 (2006).
34 Ward, A., Reyes, C. L., Yu, J., Roth, C. B. & Chang, G. Flexibility in the ABC transporter MsbA: Alternating access with a twist. *Proc. Natl. Acad. Sci. U. S. A.* **104**, 19005-19010, doi:0709388104 [pii] 10.1073/pnas.0709388104 (2007).
35 Dawson, R. J. & Locher, K. P. Structure of a bacterial multidrug ABC transporter. *Nature* **443**, 180-185, doi:nature05155 [pii] 10.1038/nature05155 (2006).

36 Fan, C., Kaiser, J. T. & Rees, D. C. A structural framework for unidirectional transport by a bacterial ABC exporter. *Proc. Natl. Acad. Sci. U. S. A.* **117**, 19228-19236, doi:10.1073/pnas.2006526117 (2020).
37 Chaptal, V. *et al.* Substrate-bound and substrate-free outward-facing structures of a multidrug ABC exporter. *Sci Adv* **8**, eabg9215, doi:10.1126/sciadv.abg9215 (2022).

Methods

Synthesis of compounds and analysis

The synthesis route and compound numbers are shown in Extended Data Fig. 1. All organic reactions were carried out under anhydrous conditions and argon atmosphere, unless otherwise noted. Reagents were purchased at the highest commercial quality and used without further purification. NMR spectra were acquired using Bruker DRX-300 or Bruker AV-600 instruments, and chemical shifts (δ) are reported in parts per million (ppm), which were calibrated using residual undeuterated solvent as an internal reference. High-resolution mass spectra (HRMS) were recorded on an Agilent Technologies 6230 TOF LC/MS with a Dual AJS ESI ion source. For flash column chromatography, the stationary phase was 60Å silica gel.

General procedure for the synthesis of *N*-Boc-(*S*)-amino thioamides 1 and 2

To a solution of *N*-Boc-(*S*)-amino acid (1.0 g, 5.20 mmol) in THF (20 mL) at 0 ºC was added triethylamine (0.8 mL, 5.80 mmol) and ethyl chloroformate (1.1 mL,10.92 mmol). The reaction mixture was stirred for 30 min before the addition of aqueous ammonium hydroxide (20 mL). The reaction mixture was stirred for a further 10 min. The mixture was extracted with ethyl acetate (EtOAc), and the organic layer was washed with brine and dried over anhydrous Na_2SO_4, then concentrated under reduced pressure to give *N*-Boc-(*S*)-amino amide as a white solid. The residue was redissolved in THF, Lawesson's reagent (3.0 g, 5.20 mmol) was added, and the reaction mixture was stirred at 50 ºC for 12 h. After solvent removal, the residue was redissolved in EtOAc. The organic layer was washed with 1% NaOH, H_2O, and brine, then dried over anhydrous Na_2SO_4 and concentrated under reduced pressure. The resulting residue was purified by silica gel column

chromatography using EtOAc/hexane (1:1) to give *N*-Boc-(*S*)-amino thioamide **1** or **2** as a yellow solid.

Synthesis of thiazole ester 3

A solution of thioamide **1** (2.0 g, 9.80 mmol) dissolved in dimethoxyethane (DME, 20 mL) was cooled to –20 ºC, followed by addition of $KHCO_3$ (7.84 g, 78.4 mmol) under inert atmosphere. The suspension was stirred for 15 min, followed by addition of ethyl bromopyruvate (3.6 mL, 29.4 mmol). The reaction mixture was further stirred for 1 h while it warmed from –20 ºC to room temperature (rt). The reaction mixture was cooled to –20 ºC again, and a solution of trifluoroacetic anhydride (5.90 mL, 39.2 mmol) and lutidine (9.7 mL, 83.3 mmol) in DME was added dropwise. The reaction mixture was allowed to warm from 0 ºC to rt and was stirred at rt for 12 h. After solvent removal, the residue was redissolved in EtOAc, and the organic layer was washed with brine, dried over anhydrous Na_2SO_4, and concentrated under reduced pressure. The resulting residue was purified by silica gel column chromatography using EtOAc/hexane (1:1) as the mobile phase, affording the thiazole ester **3** (2.0 g, 69%) as a yellow solid. MS (ESI) m/z 301 $[M+H]^+$; HRMS: calcd for $C_{13}H_{20}N_2O_4S$ $(M+H)^+$ 301.1143 found 301.1213. ^{1}H NMR (600 MHz, $CDCl_3$) δ 8.07 (s, 1H), 5.22 (s, 1H), 5.11 (s, 1H), 4.41 (q, J = 7.1 Hz, 2H), 1.62 (d, J = 6.9 Hz, 3H), 1.44 (s, 9H), 1.39 (t, J = 7.1 Hz, 3H). ^{13}C NMR (150 MHz, $CDCl_3$) δ 161.50, 147.36, 61.58, 28.45, 21.94, 14.51.

Synthesis of thiazole ester 4

4 was synthesized from thioamide **2** (1.0 g, 2.80 mmol) according to the same procedure described for the synthesis of compound **3.** Thiazole ester **4** (1.0 g, 79%) was obtained as a yellow solid. MS

(ESI) m/z 453 $[M+H]^+$; HRMS: calcd for $C_{21}H_{28}N_2O_5S_2$ $(M+H)^+$ 453.1439 found 453.1524. ^1H NMR (600 MHz, $CDCl_3$) δ 8.10 (s, 1H), 7.20 (d, J = 8.6 Hz, 2H), 6.83 (d, J = 8.6 Hz, 2H), 5.58 (s, 1H), 5.21 (s, 1H), 4.41 (q, J = 7.1 Hz, 2H), 3.79 (s, 3H), 3.53 (s, 2H), 3.17 – 2.95 (m, 2H), 1.46 (s, 9H), 1.39 (d, J = 7.1 Hz, 3H). ^{13}C NMR (150 MHz, CDCl3) δ 161.38, 158.93, 147.52, 130.23, 129.72, 127.73, 114.16, 61.62, 55.40, 52.43, 36.44, 36.20, 28.43, 14.50, 14.26.

Synthesis of dipeptide 8

To a solution of compound **3** (0.45g, 1.46 mmol) in dichloromethane (DCM, 10 mL) was added trifluoroacetic acid (TFA, 3.3 mL). The reaction mixture was stirred at rt for 1 h. The solvent was removed under reduced pressure to give the thiazole amine **5** in quantitative yield. Compound **3** (0.50 g, 1.66 mmol) was dissolved in a mixture of THF/MeOH/H_2O (3:1:1). Then NaOH (0.532 g, 13.3 mmol) was added, and the reaction mixture was stirred at rt for 1 h. After removing the solvent at reduced pressure, the residue was redissolved in EtOAc. The organic layer was washed with brine, dried over anhydrous Na_2SO_4, and concentrated in vacuo to give thiazole acid **6**. The resulting thiazole acid **6** (0.40 g, 1.46 mmol) was dissolved in anhydrous DMF (5 mL). HOBt (0.670 g, 4.38 mmol), HBTU (1.66 g, 4.38 mmol), and thiazole amine **5** (1.50 mmol, dissolved in DMF) were added sequentially. To this mixture was added iPr_2EtN (1.25 mL, 7.2 mmol) with stirring at rt under N_2 for 12 h. Upon completion, the reaction was quenched with aqueous HCl (1 M). The solution was diluted with EtOAc, washed with saturated $NaHCO_3$ solution and brine, dried over Na_2SO_4, and filtered. The solvent was then removed in vacuo, and the residue was subjected to column chromatography on silica gel to

provide the dipeptide **8** (0.560 g, 84%) as a white solid. MS (ESI) m/z 455 $[M+H]^+$; HRMS: calcd for $C_{19}H_{26}N_4O_5S_2$ $(M+H)^+$ 455.1344 found 455.1422. ^{1}H NMR (600 MHz, $CDCl_3$) δ 8.09 (s,1H), 8.03 (s, 1H), 7.86 (dd, J = 8.5, 3.4 Hz, 1H), 5.59 (tt, J = 8.7, 6.1 Hz, 1H), 5.10 (d, J = 37.7 Hz, 2H), 4.41 (q, J = 7.1 Hz, 2H), 1.79 (d, J = 7.0 Hz, 2H), 1.61 (d, J = 6.8 Hz, 2H), 1.45 (s, 9H), 1.39 (t, J = 7.1 Hz, 3H). ^{13}C NMR (150 MHz, $CDCl_3$) δ 173.18, 173.15, 160.60, 149.23, 147.30, 147.28, 127.59, 127.58, 123.98, 61.61, 47.27, 47.22, 28.46, 21.19, 21.16, 14.50.

Synthesis of linear tripeptide 10

Reaction of dipeptide **8** (0.50 g, 1.10 mmol) with TFA (3.3 mL) in DCM (15 mL) afforded the amine **9** in quantitative yield. Compound **4** (0.50 g, 1.10 mmol) was dissolved in a mixture of THF/MeOH/H_2O (3:1:1). NaOH (0.40 g, 8.84 mmol) was added, and the reaction mixture was stirred at rt for 1 h. After removing the solvent at reduced pressure, the residue was redissolved in EtOAc. The organic layer was washed with brine, dried over anhydrous Na_2SO_4, and concentrated in vacuo to give thiazole acid **7**. The resulting thiazole acid **7** (0.40 g, 0.94 mmol) was dissolved in anhydrous DMF (5 mL), then HOBt (0.431 g, 2.82 mmol), HBTU (1.06 g, 2.82 mmol), and dipeptide amine **9** (1.10 mmol, dissolved in DMF) were added. To this mixture was added iPr_2EtN (1.25 mL, 7.2 mmol) with stirring at rt under N_2 for 12 h. Upon completion, the reaction was quenched with aqueous HCl (1 M). The solution was diluted with EtOAc, washed with saturated $NaHCO_3$ solution and brine, dried over Na_2SO_4, and filtered. The solvent was then removed in vacuo, and the residue was subjected to column chromatography on silica gel to provide the linear tripeptide **10** (0.430 g, 60%) as a white solid. MS (ESI) m/z 761 $[M+H]^+$;

HRMS: calcd for $C_{33}H_{40}N_6O_7S_4$ $(M+H)^+$ 761.1841 found 761.1911. ^{1}H NMR (600 MHz, $CDCl_3$) δ 8.10 (s, 1H), 8.08 (s, 1H), 8.06 (s, 1H), 7.89 (d, J = 8.2 Hz, 1H), 7.70 (d, J = 8.1 Hz, 1H), 7.16 (d, J = 8.6 Hz, 2H), 6.80 (d, J = 8.6 Hz, 2H), 5.58 (tt, J = 15.2, 7.1 Hz, 2H), 5.44 (s, 1H), 5.17 (s, 1H), 4.41 (q, J = 7.1 Hz, 2H), 3.76 (s, 3H), 3.60 – 3.53 (m, 2H), 3.00 (td, J = 12.0, 5.5 Hz, 2H), 1.79 (dd, J = 7.0, 3.9 Hz, 6H), 1.46 (s, 9H), 1.39 (t, J = 7.1 Hz, 3H). ^{13}C NMR (150 MHz, $CDCl_3$) δ 173.20, 172.77, 160.54,149.24, 147.28, 130.17, 129.49, 127.59, 124.59, 124.33, 114.17, 61.62, 55.39, 47.31, 47.28, 38.77, 36.27, 28.44, 21.22, 21.17, 14.50.

Synthesis of cyclic peptide 11

Linear tripeptide **10** (0.20 g, 0.26 mmol) was treated with NaOH (0.084 g, 2.10 mmol) to hydrolyze the ethyl ester, then with TFA (1 mL) to remove the *N*-*t*-Boc protective group. The residue (0.164 g, 0.25 mmol) was dissolved in a mixture of DMF/DCM (2:1, 30 mL), then a solution of PyBop (0.299 g, 0.57 mmol) and 4-dimethylaminopyridine (0.143g, 1.17 mmol) in DMF/DCM (2:1, 44 mL) was added slowly over 10 h using a syringe pump. The reaction mixture was washed with aqueous HCl (1 M), saturated $NaHCO_3$, and brine, and dried over Na_2SO_4. The solvent was then removed in vacuo. The residue was purified by column chromatography on silica gel to give cyclic peptide **11** (0.102 g, 58%) as a white solid. MS (ESI) m/z 615 $[M+H]^+$; HRMS: calcd for $C_{26}H_{26}N_6O_4S_4$ $(M+H)^+$ 615.0898 found 615.0950. ^{1}H NMR (600 MHz, $CDCl_3$) δ 8.70 (d, J = 7.9 Hz, 1H), 8.65 (dd, J = 13.4, 7.7 Hz, 2H), 8.18 (s, 1H), 8.16 (s, 1H), 8.15 (s, 1H), 7.28 (d, J = 8.6 Hz, 2H), 6.85 (d, J = 8.6 Hz, 2H), 5.68 – 5.54 (m, 3H), 3.79 (s, 3H), 3.78 – 3.72 (m, 2H), 3.13 (dd, J = 13.8, 4.8 Hz, 1H), 2.84 (dd, J = 13.9, 8.4 Hz, 1H), 1.73

(d, J = 6.8 Hz, 6H). 13C NMR (150 MHz, $CDCl_3$) δ 171.46, 171.44, 159.74, 158.96, 149.04, 148.92, 130.36, 129.82, 124.78, 124.40, 124.17, 114.17, 114.13, 55.43, 53.57, 51.12, 47.57, 47.39, 38.19, 36.27, 25.13.

Synthesis of AAC-DNPT

To a solution of cyclic peptide **11** (50 mg, 0.08 mmol) in DCM (2 mL) was added 2,4-dinitrobenzenesulfenyl chloride (22 mg, 0.09 mmol) and TFA (0.018 mL, 0.24 mmol). The reaction mixture was stirred at rt for 1 h. Reaction was quenched with H_2O. The organic layer was washed with brine, dried over anhydrous Na_2SO_4, and the solvent was then removed in vacuo. The residue was purified by column chromatography on silica gel to give AAC-DNPT (32 g, 57%) as a yellow solid. MS (ESI) m/z 693 $[M+H]^+$; HRMS: calcd for $C_{24}H_{20}N_8O_7S_5$ $(M+H)^+$ 693.0058 found 693.0143. ^{1}H NMR (600 MHz, $CDCl_3$) δ 9.08 (d, J = 2.3 Hz, 1H), 8.71 (d, J = 7.5 Hz, 1H), 8.61 (dd, J = 15.0, 7.5 Hz, 2H), 8.49 (d, J = 9.0 Hz, 1H), 8.42 (dd, J = 9.0, 2.4 Hz, 1H), 8.25 (s, 1H), 8.17 (s, 1H), 8.14 (s, 1H), 5.83 (dt, J = 7.5, 5.9 Hz, 1H), 5.68 – 5.58 (m, 2H), 3.45 (d, J = 5.8 Hz, 2H), 1.75 (t, J = 6.8 Hz, 6H). ^{13}C NMR (150 MHz, $CDCl_3$) δ 171.85, 159.99, 159.66, 149.61, 148.87, 148.18, 145.83, 145.53, 145.29, 128.91, 127.63, 125.10, 124.91, 124.34, 121.77, 50.87, 47.55, 44.91, 25.08.

Expression and purification of single-cysteine mutants of Pgp

Single-Cys mutant constructs of murine Pgp (Mdr1a, accession number NM_011076, GenBank JF83415) were generated on a Cysless Pgp (CL-Pgp) background in the *Pichia pastoris* pPIC-CL-

mdr1a expression vector[38] by site-directed mutagenesis. For cryoEM structural studies of L335C and V978C, we further substituted the catalytic carboxylates in both NBDs to glutamines, E552Q/E1197Q, to generate ATP hydrolysis-deficient mutants. The Pgp construct used in this study contained C-terminal hexahistidine and Twin-Strep purification tags [40]. Large-scale Pgp biomass production in *Pichia pastoris* and microsomal membrane preparations were conducted according to published protocols[38,39].

For ATPase activity measurement and MS analysis, we purified Pgp in the presence of n-dodecyl-D-maltopyranoside (DDM) supplemented with the lipid 1-palmitoyl-2-oleoyl-sn-glycero-3-phosphoethanolamine (POPE). Briefly, microsomes were resuspended in 20 mM Tris (pH 8.0), 20 mM imidazole, 20% glycerol, 500 mM NaCl, protease inhibitors (10 μg/mL leupeptin and pepstatin A, 2.5 μg /mL chymostatin,1 mM PMSF), 0.2 mM tris(2-carboxyethyl)phosphine with 1% DDM for 60 min at 4 ºC. After centrifugation at 38,000 × *g* for 30 min, Pgp was purified from the supernatant using Ni-NTA affinity chromatography in Buffer A (50 mM Tris pH 8.0, 150 mM NaCl, 20% glycerol) supplemented with 0.067% DDM, 0.04% sodium cholate, and 0.1 mg/mL POPE, and with 20 mM imidazole for wash buffer or 200 mM imidazole for elution buffer. The eluate from Ni-NTA was concentrated for further purification by size exclusion chromatography on a Superdex 200 Increase 10/300 column using 20 mM Tris pH 7.5, 150 mM NaCl, 0.067% DDM, 0.04% sodium cholate, and 0.1 mg/ml POPE.

For cryoEM structural determination, we purified Pgp in a mixture of lauryl maltose neopentyl glycol (LMNG) and cholesteryl hemisuccinate (CHS). Briefly, after the solubilization of microsomes in DDM, Pgp was purified from the supernatant using Ni-NTA affinity chromatography in Buffer A supplemented with 0.02% LMNG, and 0.004% CHS. The eluate from

Ni-NTA was applied to pre-equilibrated Strep-Tactin Superflow resin and incubated at 4 °C for 1 h. Flow-through was removed, and the resin was washed with Buffer A in the presence of 0.02% LMNG, and 0.004% CHS. Pgp was eluted with the same buffer containing 2.5 mM desthiobiotin. The eluate from Strep-Tactin was concentrated for further purification by size exclusion chromatography on a Superdex 200 Increase 10/300 column using a detergent-free buffer containing 20 mM Tris pH 7.5 and 200 mM NaCl.

Crosslinking between single cysteine mutants of Pgp and AAC-DNPT

The covalent Pgp complexes were typically prepared by the reaction of Pgp (3-5 mg/mL) with 10-fold excess of AAC-DNPT at room temperature for 30 min. L971C labeling was conducted in the presence of MgATP (10 mM). The DNPT color formation was visualized by eye or monitored by UV-visible spectroscopy (λ_{max} = 408 nm, ε = 13800 M^{-1} cm^{-1}). For mass spectrometric analysis, AAC-labeled Pgp sample was passed through a PD-10 Sephadex G-25 desalting column to remove excess ligand, and the eluate was further treated by addition of cysteine (5 mM) before performing trypsin digestion.

ATPase activity assay.

ATPase activity of Pgp, with or without AAC labeling, was measured at 37 °C using an enzyme-coupled ATP regeneration system[41]. Briefly, 1 μg Pgp was added to 100 μL of ATP cocktail (50 mM Tris, pH 7.5, 12 mM $MgCl_2$, 6 mM phosphoenolpyruvate, 1 mM NADH, 10 units lactate dehydrogenase, 10 units pyruvate kinase, and 10 mM ATP). The rate of ATP hydrolysis was determined by the decrease in NADH absorbance at 340 nm using a microplate reader (Filtermax F5). Verapamil was added from stocks in water, QZ-Ala, AAC-DNPT, FK506 and valinomycin

were added from stocks in DMSO such that the final DMSO concentration was ≤ 1%. ATPase activity was calculated as described previously[42]. To analyze the activities of Pgp mutants (L335C, V978C, and L971C, with CL-Pgp as control) with varying concentrations of AAC-DNPT (0-20 μM), we incubated Pgp with AAC-DNPT for 15 min at room temperature prior to the addition of ATP to initiate the ATPase reaction.

Trypsin digestion of Pgp.

Ten μL of 5 mg/mL Pgp, with or without AAC labeling, was added to an S-Trap micro column (Farmingdale NY). Then 15 μL of 100 mM triethylammonium bicarbonate (TEAB) buffer (pH 7.5) containing 10% sodium dodecyl sulfate (SDS) was drawn and mixed with Pgp protein by pipette. Then 2.5 μL of 10% (v/v) H_3PO_4 in water was added to the S-Trap. After 10 min incubation, 165 μL of binding solution (100 mM TEAB in MeOH/H_2O 9:1 (v/v), pH 7.1) was added to the acidified Pgp protein. After 10 min incubation, the S-Trap was seated in a 1.5 mL tube and centrifuged at 4000 × *g* for 2 min until all solution had passed through the S-Trap membrane. The flow-through liquid was drawn back and centrifuged again. After addition of 150 μL of binding solution, the S-Trap was centrifuged at 4000 × *g* for 2 min to wash the protein. The flow-through liquid was removed, and this washing procedure was repeated three times. Trypsin (4 μg, at an enzyme/protein ratio of 1:12.5, w/w) was added to the S-Trap and mixed well. The S-Trap was capped loosely to limit evaporation, then incubated in a dry incubator at 37°C for overnight digestion. After digestion was completed, the resulting peptides were eluted by adding 40 μL of H_2O containing 0.2% formic acid (FA), and centrifuging at 4000 × *g* for 2 min. The flow-through liquid was transferred back to be centrifuged again. Then 35 μL of CH_3CN/H_2O/FA (80:20:0.2%) was added, and the S-Trap was centrifuged at 4000 × *g* for 2 min. The eluted peptides were collected for LC-MS analysis.

LC-MS analysis

The LC-MS setup consisted of an ultra-performance liquid chromatography instrument (UPLC, Waters, Milford, MA) coupled with a high-resolution Orbitrap Q Exactive mass spectrometer (Thermo Scientific, San Jose, CA). A reversed-phase column (BEH C18, 1.0 mm × 100 mm, 1.8 μm) was used for separation. The injection volume was 5 μL per analysis. For gradient elution (0-95% CH_3CN with 0.1% FA in water), the mobile phase flow rate was 30 μL/min. The Orbitrap mass spectrometer was equipped with a heated electrospray ionization (HESI) source. The rate of sheath gas flow was 10 L/h and the applied ionization voltage was +4 kV. The ion transfer inlet capillary temperature was kept at 250 °C. Mass spectra were acquired using Thermo Xcalibur (3.0.63) software. The scan mode was set to full scan MS^1, followed by data-dependent MS^2 acquisition. The resolution of full scan MS^1 was 70k and the automatic gain control (AGC) target was set to 5e5. For MS^2 acquisition, the resolution was 17.5k, and AGC target was 2e4. The 20 most abundant ions (+2 to +6 ions) were selected to fragment with a normalized collision energy of 30%.

MDCK-MDR1 transport assay

The Madin Darby Canine Kidney (MDCK) epithelial cells stably transfected with the human *MDR1* gene forms a confluent monolayer, which is widely adopted to evaluate if a compound is subject to Pgp efflux based on the permeability measurement in both directions[43]. The MDCK-MDR1 permeability assay for QZ-Ala was conducted by Bioduro-Sundia Inc. (San Diego, CA). Briefly, 5 μM QZ-Ala in the absence or presence of 10 μM cyclosporin A was added to either the apical (A) or the basolateral (B) side and the amount of permeation was determined on the other

side of the monolayer by LC-MS/MS. The efflux ratio ($R_E = P_{app}$ (B-A) to P_{app}(A-B)) for QZ-Ala was determined following standard protocols. An $R_E > 2.0$ generally indicates a substrate for Pgp.

G72A mutagenesis and drug resistance assays

G72A mutation was conducted on the mouse CL-Pgp template in the pVT expression vector (pVT-CL-*mdr1a*)[44]. First, the three N-glycosylation sites N82/N87/N90 that were previously substituted by Gln for X-ray crystallography were restored to the original codons 5'-AACgtgtccaagAACagtactAAT-3' by QuickChange site-directed mutagenesis. The G72A mutation was then added by a second round of site-directed mutagenesis, and the full-length open reading frame sequenced to confirm no other unwanted mutation was present. Plasmids from three individual clones, together with WT-Pgp and CL-Pgp as well as pVT "empty" vector controls were transformed into *S. cerevisiae* JPY201 (MATa ura3 Δste6::HIS3) cells for expression and functional assays that were performed essentially as previously described[44]. Briefly, 10 ml yeast cultures were grown overnight in uracil-deficient minimal medium, diluted to OD_{600}=0.05 in YPD medium [1% (w/v) yeast extract/2% (w/v) peptone/2% (w/v) glucose], and seeded into 96-well plates containing YPD alone or YPD plus 40 μM doxorubicin, 50 μM FK506 or 100 μM valinomycin. Samples were grown in triplicate wells at 30ºC for up to 40 h, and yeast cell growth was monitored by measuring the OD_{600} at 2 h increments in a microplate reader (Benchmark Plus, BioRad). The remainder of the 10 ml cultures was used to assess Pgp expression by Western blot analysis of microsomal membrane preparations using the monoclonal C219 anti-Pgp antibody.

For ATPase assays, the three N-glycosylation sites were restored in the *P. pastoris* pPIC-CL-*mdr1a* expression vector and the G72A mutant introduced by site-directed mutagenesis. For cry-EM, L335C was added to the G72A mutant by mutagenesis; the integrity of the open reading frame was confirmed by DNA sequencing after each round of mutagenesis. G72A and G72A/L335C

mutant proteins were purified from *P. pastoris* microsomal membranes as described for single Cys mutants. Bars in Fig. 3 represent the mean of ≥3 independent experiments ± SEM; two way ANOVA with post hoc Bonferroni tests identified those pairs with very highly significant differences ($p < 0.001$).

EM sample preparation

After shipment, quality control of the samples was performed by collecting negative stain EM images on a Tecnai G^2 Spirit TWIN TEM (FEI) [45]. For cryoEM, all samples were adjusted to 3.5 mg/mL in 50 mM Tris, pH 7.5 and 200 mM NaCl. OF335 was obtained after reaction with a 4-fold excess of AAC-DNPT; OF978C and 971C were obtained with 10-fold molar excess for 30 min at room temperature. To trigger NBD-dimerization, the QQ constructs were then incubated with 5 mM MgATP for 1 h at room temperature prior to grid preparation. For OF971, 5 mM Mg^{2+}ATP/Vi was added to the sample and incubated for 1 h at room temperature. Freezing protocol was followed as previously described[46]. All samples were vitrified on freshly glow-discharged CF-1.2/1.3 TEM grids (Protochips, USA) with a Vitrobot Mark IV (Thermo Fisher Scientific, Inc., USA) at 100% humidity and 4 °C, with a nominal blot force of –2 and a blotting time of 12 s. Grids were plunged into liquid ethane and stored in liquid nitrogen until further use.

EM data acquisition and processing

The data sets for OF978 and OF971 were acquired on a Titan Krios G4, operated at 300kV and equipped with a Selectris X imaging filter and a Falcon 4 direct electron detector (all Thermo Fisher Scientific, USA). Datasets were obtained using automation strategies of EPU software v2.13 (Thermo Scientific) at a nominal magnification of 215,000, corresponding to a calibrated pixel size of 0.573 Å. The camera was operated in electron counting mode, and the data were saved

in electron-event representation (EER) format. All other data sets were obtained on a Titan Krios G3i (Thermo Fisher Scientific, USA), using automation strategies of EPU 2.9 or newer, equipped with a Gatan BioQuantum K3 Imaging Filter (Gatan, USA) in electron counting mode. The nominal magnification was 105,000 corresponding to a calibrated pixel size of 0.837 Å. The exposure time for all data sets was ~4s, and the total dose was 70 $e^-/Å^2$ (Selectris X - Falcon 4) or 75 $e^-/Å^2$ (BioQuantum K3). Quality of the data was monitored during collection using cryoSPARC live v3.2.0 and v3.3.1[47]. Details about number of collected images and picked particles, as well as number of particles in the final map and resolutions are listed in Extended Data Table 1.

For data processing for IF335, the initial model was obtained using cryoSPARC v3.2.0. Further processing, including 3D classifications and refinements, was obtained in Relion 3.1[48]. For the final refinement, particles and map were transferred back to cryoSPARC v3.2.0 to run a Non-Uniform Refinement (NUR)[49]. All other data sets were processed in cryoSPARC v3.3.1. Particles were picked broadly with the blob picker, and the best classes were selected for further processing. Sorting of the particles was achieved by multiple heterogenous refinements and NUR. Global and local CTF refinements[50] were performed toward the end of the processing pipeline, followed by another round of NUR. An exemplary processing pathway is provided in Extended Data Fig. 10. Processing results for all structures are shown in Extended Data Fig. 6.

For all data sets, the images were repicked with the Topaz[51] picker, and this increased the resolution for all three maps from the OF335 data set. For all other data sets, no improvement of the maps could be achieved with this approach. Density modification with *phenix.resolve_cryo_em*[52] was carried out using two half-maps together with the FSC-based resolution and the molecular masses of the molecules. This procedure resulted in significant

improvement of the map qualities. The density-modified map of OF335-1lig was used for Extended Data Fig. 7.

Model building

For all datasets, the structures of Pgp in the inward and outward conformations (PDBID: 4Q9I and 6C0V, respectively) were used as templates. All structures were manually edited in COOT[53] and refined using *phenix.real_space_refine,* in combination with rigid-body refinement[54] and several rounds of rebuilding in COOT. A quality check of all structures with MolProbity[55] indicated excellent stereochemistry with 93.1% - 98.1% of the non-glycine and non-proline residues found in the most-favored region, and 0.00% - 0.09% outliers (all-atom clashscore: 9.29 – 15.76). Refinement and validation statistics are summarized in Extended Data Table 1. Figures were drawn with ChimeraX[56] and PyMOL (The PyMOL Molecular Graphics System, Version 2.0, Schrödinger, LLC).

Molecular dynamics simulations

Molecular dynamics simulations were performed starting from the structures OF978-1lig and OF335-2lig embedded in a patch of lipid bilayer. The bound cholesterol hemisuccinate molecules in the cryoEM structures were replaced with cholesterol in the same binding poses. Bound magnesium ions and ATP were also retained. The crosslinked ligands were removed and the crosslinking cysteine was replaced by the amino acid originally present at that position. No attempt was made to model the unresolved linker (residue 626-686). Instead the C-terminus of the first subunit (residue 625) was N-methylated and the N-terminus of the second subunit (residue 687) was acetylated to imitate the presence of an unstructured loop region connecting the two subunits. The structures were then inserted into a model plasma membrane and solvated using CHARMM-GUI[57,58] (composition outer leaflet: 30% CHL, 35% POPC, 35% PSM; composition inner leaflet:

30% CHL, 25% PAPC, 25 POPE, 25% POPS). All protonation states were set according to propka3[59,60]. The resulting simulation systems were placed in rectangular boxes with a size of approximately $12 \times 12 \times 17$ nm^3 and around 260,000 atoms each. The ligands were modeled using the CGenFF server[61,62] and placed into the solvated systems at their original location as in the pdb structures with the crosslink to the protein removed.

All molecular dynamics simulations were performed with the CHARMM36m forcefield[63](version july2021) including CGenFF parameters[64] (version 4.6) using gromacs[65,66] (version 2021.6). Hydrogen bond lengths were constrained using LINCS[67] in all simulations. The simulation systems were energy minimized and subsequently equilibrated in six steps while gradually releasing restraints on the positions of the heavy and backbone atoms of the protein, the lipid atoms and the ligand atoms (see Extended Data Table 2).

The production simulations were started from the last configuration of the equilibration with random initial velocities. All production simulations were performed in the NPT ensemble using a semi-isotropic Parrinello-Rahman barostat[68] with a target pressure of 1 bar and a coupling constant of 5 ps. The velocity rescale thermostat[69] with a time constant of 1 ps was used to keep the target temperature of T=400 K. We used a time step of 0.002 ps.

Additional References

38 Swartz, D. J. *et al.* Directed evolution of P-glycoprotein cysteines reveals site-specific, non-conservative substitutions that preserve multidrug resistance. *Biosci. Rep.* **34**, 297-310, doi:10.1042/BSR20140062 (2014).

39 Bai, J. *et al.* A gene optimization strategy that enhances production of fully functional P-glycoprotein in Pichia pastoris. *PloS one* **6**, e22577, doi:10.1371/journal.pone.0022577 (2011).

40 Zoghbi, M. E. *et al.* Substrate-induced conformational changes in the nucleotide-binding domains of lipid bilayer-associated P-glycoprotein during ATP hydrolysis. *J. Biol. Chem.* **292**, 20412-20424, doi:10.1074/jbc.M117.814186 (2017).
41 Urbatsch, I. L., Sankaran, B., Weber, J. & Senior, A. E. P-glycoprotein is stably inhibited by vanadate-induced trapping of nucleotide at a single catalytic site. *J. Biol. Chem.* **270**, 19383-19390 (1995).
42 Urbatsch, I. L., Tyndall, G. A., Tombline, G. & Senior, A. E. P-glycoprotein catalytic mechanism: studies of the ADP-vanadate inhibited state. *J. Biol. Chem.* **278**, 23171-23179, doi:10.1074/jbc.M301957200 (2003).
43 Brouwer, K. L. *et al.* In vitro methods to support transporter evaluation in drug discovery and development. *Clin. Pharmacol. Ther.* **94**, 95-112, doi:10.1038/clpt.2013.81 (2013).
44 Swartz, D. J. *et al.* Directed evolution of P-glycoprotein cysteines reveals site-specific, non-conservative substitutions that preserve multidrug resistance. *Biosci. Rep.* **34**, doi:10.1042/BSR20140062 (2014).
45 Gewering, T., Januliene, D., Ries, A. B. & Moeller, A. Know your detergents: A case study on detergent background in negative stain electron microscopy. *J. Struct. Biol.* **203**, 242-246, doi:10.1016/j.jsb.2018.05.008 (2018).
46 Januliene, D. & Moeller, A. Single-particle cryoEM of membrane proteins. *Methods Mol. Biol.* **2302**, 153-178, doi:10.1007/978-1-0716-1394-8_9 (2021).
47 Punjani, A., Rubinstein, J. L., Fleet, D. J. & Brubaker, M. A. cryoSPARC: algorithms for rapid unsupervised cryoEM structure determination. *Nat. Methods* **14**, 290-296, doi:10.1038/nmeth.4169 (2017).
48 Scheres, S. H. RELION: implementation of a Bayesian approach to cryoEM structure determination. *J. Struct. Biol.* **180**, 519-530, doi:10.1016/j.jsb.2012.09.006 (2012).
49 Punjani, A., Zhang, H. & Fleet, D. J. Non-uniform refinement: adaptive regularization improves single-particle cryoEM reconstruction. *Nat. Methods* **17**, 1214-1221, doi:10.1038/s41592-020-00990-8 (2020).
50 Rubinstein, J. L. & Brubaker, M. A. Alignment of cryoEM movies of individual particles by optimization of image translations. *J. Struct. Biol.* **192**, 188-195, doi:10.1016/j.jsb.2015.08.007 (2015).
51 Bepler, T., Kelley, K., Noble, A. J. & Berger, B. Topaz-Denoise: general deep denoising models for cryoEM and cryoET. *Nat. Commun.* **11**, 5208, doi:10.1038/s41467-020-18952-1 (2020).
52 Terwilliger, T. C., Ludtke, S. J., Read, R. J., Adams, P. D. & Afonine, P. V. Improvement of cryoEM maps by density modification. *Nat. Methods* **17**, 923-927, doi:10.1038/s41592-020-0914-9 (2020).
53 Emsley, P. & Cowtan, K. Coot: model-building tools for molecular graphics. *Acta Crystallogr. Section D: Biol. Crystallogr.* **60**, 2126-2132, doi:10.1107/S0907444904019158 (2004).
54 Afonine, P. V. *et al.* Real-space refinement in PHENIX for cryoEM and crystallography. *Acta Crystallogr. D Struct. Biol.* **74**, 531-544, doi:10.1107/S2059798318006551 (2018).
55 Chen, V. B. *et al.* MolProbity: all-atom structure validation for macromolecular crystallography. *Acta Crystallogr. Section D: Biol. Crystallogr.* **66**, 12-21, doi:10.1107/S0907444909042073 (2010).
56 Goddard, T. D. *et al.* UCSF ChimeraX: Meeting modern challenges in visualization and analysis. *Protein Sci.* **27**, 14-25, doi:10.1002/pro.3235 (2018).
57 Wu, E. L. *et al.* CHARMM-GUI Membrane Builder toward realistic biological membrane simulations. *J. Comput. Chem.* **35**, 1997-2004, doi:10.1002/jcc.23702 (2014).

58 Lee, J. *et al.* CHARMM-GUI input generator for NAMD, GROMACS, AMBER, OpenMM, and CHARMM/OpenMM simulations using the CHARMM36 additive force field. *J. Chem. Theory Comput.* **12**, 405-413, doi:10.1021/acs.jctc.5b00935 (2016).
59 Sondergaard, C. R., Olsson, M. H., Rostkowski, M. & Jensen, J. H. Improved treatment of ligands and coupling effects in empirical calculation and rationalization of pKa values. *J. Chem. Theory Comput.* **7**, 2284-2295, doi:10.1021/ct200133y (2011).
60 Olsson, M. H., Sondergaard, C. R., Rostkowski, M. & Jensen, J. H. PROPKA3: Consistent treatment of internal and surface residues in empirical pKa predictions. *J. Chem. Theory Comput.* **7**, 525-537, doi:10.1021/ct100578z (2011).
61 Vanommeslaeghe, K. & MacKerell, A. D., Jr. Automation of the CHARMM General Force Field (CGenFF) I: bond perception and atom typing. *J. Chem. Inf. Model* **52**, 3144-3154, doi:10.1021/ci300363c (2012).
62 Vanommeslaeghe, K., Raman, E. P. & MacKerell, A. D., Jr. Automation of the CHARMM General Force Field (CGenFF) II: assignment of bonded parameters and partial atomic charges. *J. Chem. Inf. Model* **52**, 3155-3168, doi:10.1021/ci3003649 (2012).
63 Huang, J. *et al.* CHARMM36m: an improved force field for folded and intrinsically disordered proteins. *Nat. Methods* **14**, 71–73 (2017).
64 Vanommeslaeghe, K. *et al.* CHARMM general force field: A force field for drug-like molecules compatible with the CHARMM all-atom additive biological force fields. *J. Comput. Chem.* **31**, 671-690, doi:10.1002/jcc.21367 (2010).
65 Pall, S. *et al.* Heterogeneous parallelization and acceleration of molecular dynamics simulations in GROMACS. *J. Chem. Phys.* **153**, 134110, doi:10.1063/5.0018516 (2020).
66 Abraham, M. J. *et al.* GROMACS: High performance molecular simulations through multi-level parallelism from laptops to supercomputers. *SoftwareX* **1-2**, 26-31 (2015).
67 Hess, B., Bekker, H., Berendsen, H. J. C. & Fraaije, J. G. E. M. LINCS: A linear constraint solver for molecular simulations. *J. Comput. Chem.* **18**, 1463–1472 (1997).
68 Parrinello, M. & Rahman, A. Polymorphic transitions in single crystals: A new molecular dynamics method. *J. Appl. Phys.* **52**, 7182–7190 (1981).
69 Bussi, G., Donadio, D. & Parrinello, M. Canonical sampling through velocity rescaling. *J. Chem. Phys.* **126**, 014101 (2007).
70. E. Chovancova *et al.*, CAVER 3.0: a tool for the analysis of transport pathways in dynamic protein structures. *PLoS Comput. Biol.* **8**, e1002708 (2012).
71. A. C. Wallace, R. A. Laskowski, J. M. Thornton, LIGPLOT: a program to generate schematic diagrams of protein-ligand interactions. *Protein Eng.* **8**, 127-134 (1995).

Acknowledgments

We thank J.-H. Leung, W.-H. Lee, and A. Ward for early contributions, C. Katz for technical assistance, S. Welsch and S. Prinz for support during the cryoEM data collection, W. Kühlbrandt for generous access to the cryoEM facilities in Frankfurt and general support, and W. Kühlbrandt and I. Wilson for critical reading and editing of the manuscript. This work was supported by National Institute of General Medical Sciences R01 GM118594 (QZ) and GM141216 (ILU), the Deutsche Forschungsgemeinschaft (DFG) Sonderforschungsbereich 944 and 1557 and INST 190/196 (AM) , the Bundesministerium für Bildung und Forschung (BMBF) 01ED2010 (AM), the Max Planck Society (HJ, GH,AM & TG), and the South Plains Foundation (ILU).

Author contributions

TG performed cryoEM and single particle analysis with help from DJ and AM. DW conducted ligand synthesis and crosslinking, identified Pgp single Cys mutants, performed biochemical characterization, and optimized and prepared Pgp samples for mass spectrometry and cryoEM studies under the supervision of QZ. PZ performed mass spectrometric characterization of crosslinking under the supervision of HC. KP built molecular models with help from TG and AM. JZ expressed Pgp mutants, and NT assayed G72A function under the supervision of ILU. HJ conducted molecular dynamics simulations under the supervision of GH. QZ and ILU conceived the Pgp labeling experiments and designed and tested the mutations. AM designed and supervised the cryoEM research. AM, TG and DJ interpreted the cryoEM structural data with significant input from QZ. QZ conceived and initiated the project, designed the research, and coordinated collaborations. The manuscript was written by TG, DW, DJ, ILU, QZ and AM. All authors carefully discussed and interpreted the data.

Competing interests

Authors declare that they have no competing interests.

Data availability

Supplementary Information is available for this manuscript. All cryoEM density maps have been deposited in the Electron Microscopy Data Bank under accession numbers EMD-14754, EMD-14755, EMD-14756, EMD-14758, EMD-14759, EMD-14760, EMD-14761 and EMD-17630. Atomic coordinates for the atomic models have been deposited in the Protein Data Bank under accession numbers 7ZK4, 7ZK5, 7ZK6, 7ZK8, 7ZK9, 7ZKA, 7ZKB and 8PEE.

Additional Information

Correspondence and requests for materials should be addressed to Q.Z. or A.M.

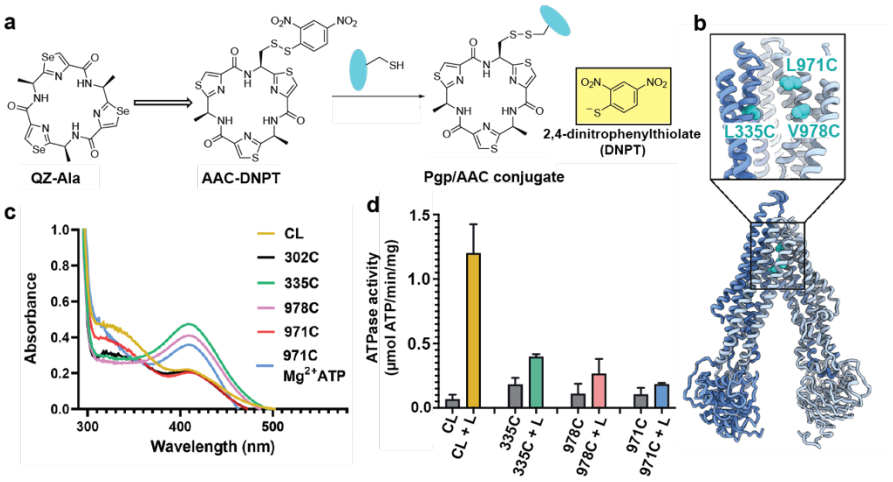

Fig. 1. Covalent ligand design for Pgp transport studies. (a) Design of AAC-DNPT, a derivative of the cyclic peptide QZ-Ala, for disulfide crosslinking with single-cysteine mutants of Pgp; yellow product DNPT used as readout. **(b)** Positions of L335 (TM6), V978 and L971 (TM12) in Pgp, residues targeted for cyclic peptide labeling. **(c)** Monitoring covalent reaction between AAC-DNPT and cysteine mutants (+/- Mg^{2+}ATP) by UV-visible spectrometry; CL-Pgp and I302C were included as negative controls. **(d)** ATPase activities of L335C, V978C, and L971C before and after crosslinking with AAC-DNPT; CL-Pgp was used as a control. Data are averaged from triplicate measurements with standard error bars.

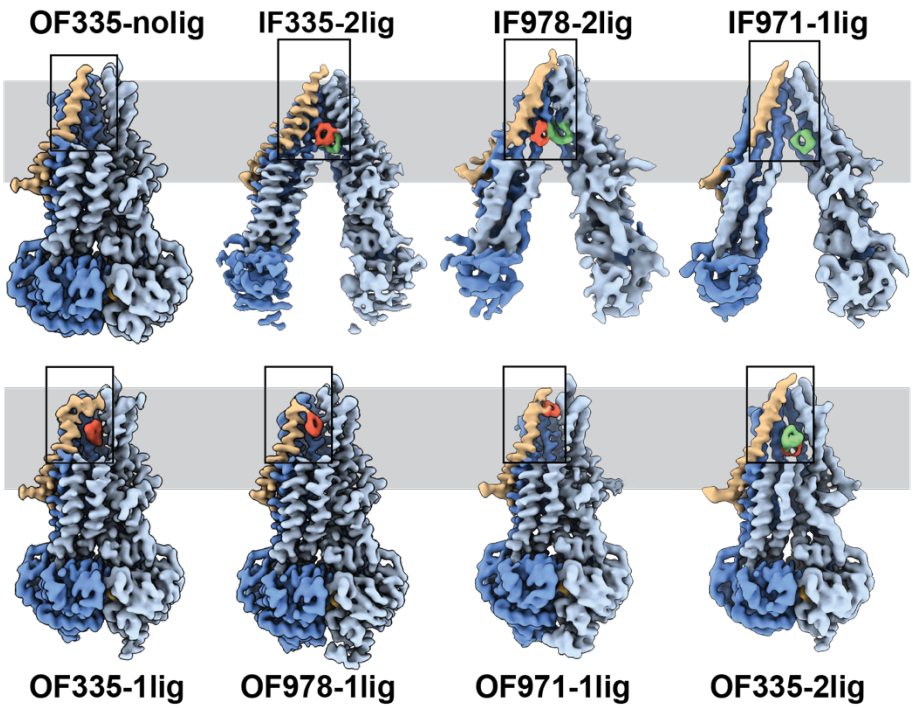

Fig. 2. High-resolution structures of Pgp with bound ligands. For all mutants, IF and OF structures were obtained, with ligands revealed in the transmembrane region (grey shadow). For Pgp335 three different OF conformations were detected in one data set (OF335-nolig, OF335-1lig, OF335-2lig). To display the binding sites, the upper halves of TM 2,10,11 and 12 were removed from the densities. For the IF structures, TM9 was also removed for clarity. TM1 is shown in brown, with the covalently bound ligand in red and the non-crosslinked in green**.** Significant conformational changes were observed among these structures from which a further zoom-in of TM1 (black box region) was shown in Fig. 4 and Extended Data Fig. 8.

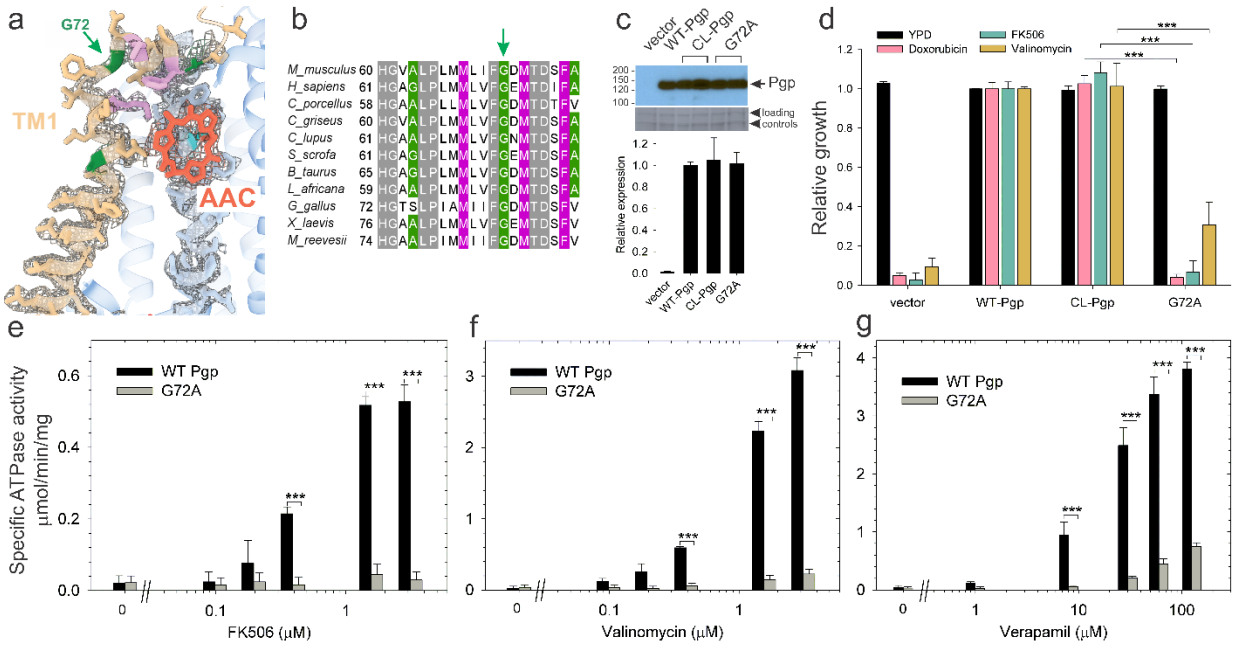

Fig. 3. Functional characterization of G72A mutant. (a) TM1 breaks at the G72 position in the mid-transport states of Pgp. Shown is a close-up view of TM1 (brown) with side chain densities, the G72 position (green arrow), and the adjacently bound cyclic peptide AAC (red sticks) in the OF335-1lig structure. **(b)** Sequence alignment of TM1 in vertebrate Pgps including the highly conserved G72 residue (green arrow). **(c)** Level of expression of the G72A mutant relative to the WT- and CL-Pgp in *S. cerevisiae* cultures derived from the western blot analysis. **(d)** In vivo activity of the G72A mutant. The growth resistance of *S. cerevisiae* cultures transformed with either vector control plasmid, WT-Pgp, CL-Pgp, or the G72A mutant against several fungicides (doxorubicin, FK506, and valinomycin) relative to the YPD medium only (black bar) were analyzed. Compared to WT-Pgp and CL-Pgp, the G72A mutant severely compromised growth resistance against the tested drugs (p-values of <0.001 are indicated by ***). **(e-g)** ATPase activity of the purified G72A mutant. While basal ATP hydrolysis rates (in the absence or at low concentrations of drug) were indistinguishable between WT and G72A mutant proteins,

stimulation of the ATPase activities by 1-3 μM FK506, 1-3 μM valinomycin, or 30-130 μM verapamil were severely impaired (p-values of <0.001 are indicated by ***).

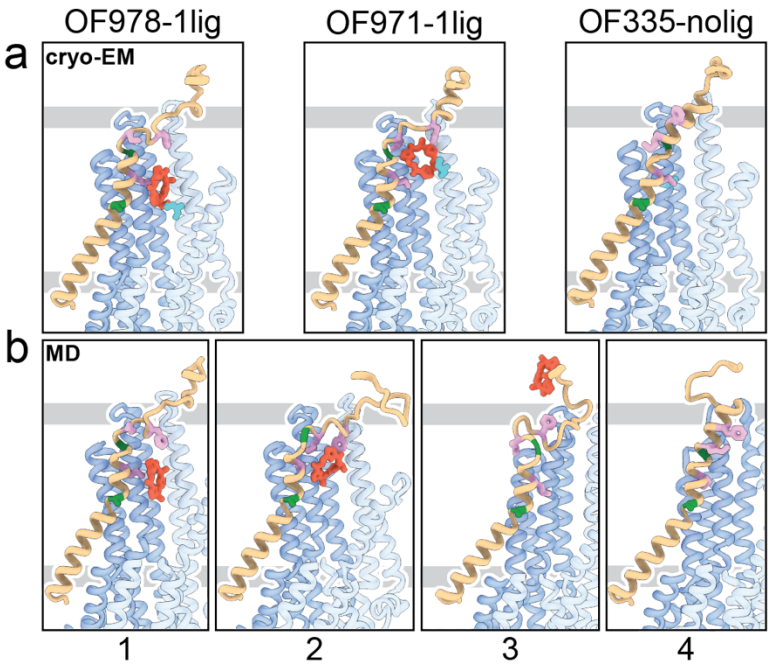

Fig. 4. Tracing the substrate movement in Pgp. Structures of OF Pgp from cryoEM **(a)** aligned with four snapshots from MD simulations **(b)** of substrate transport and release. TM1 is rendered in brown, with A63 and G72 in green, and M68, M74, and F78 in plum. The cyclic peptide is shown as red sticks. Significant conformational changes were observed for TM1 along with the upward movement and release of the substrate from OF Pgp.

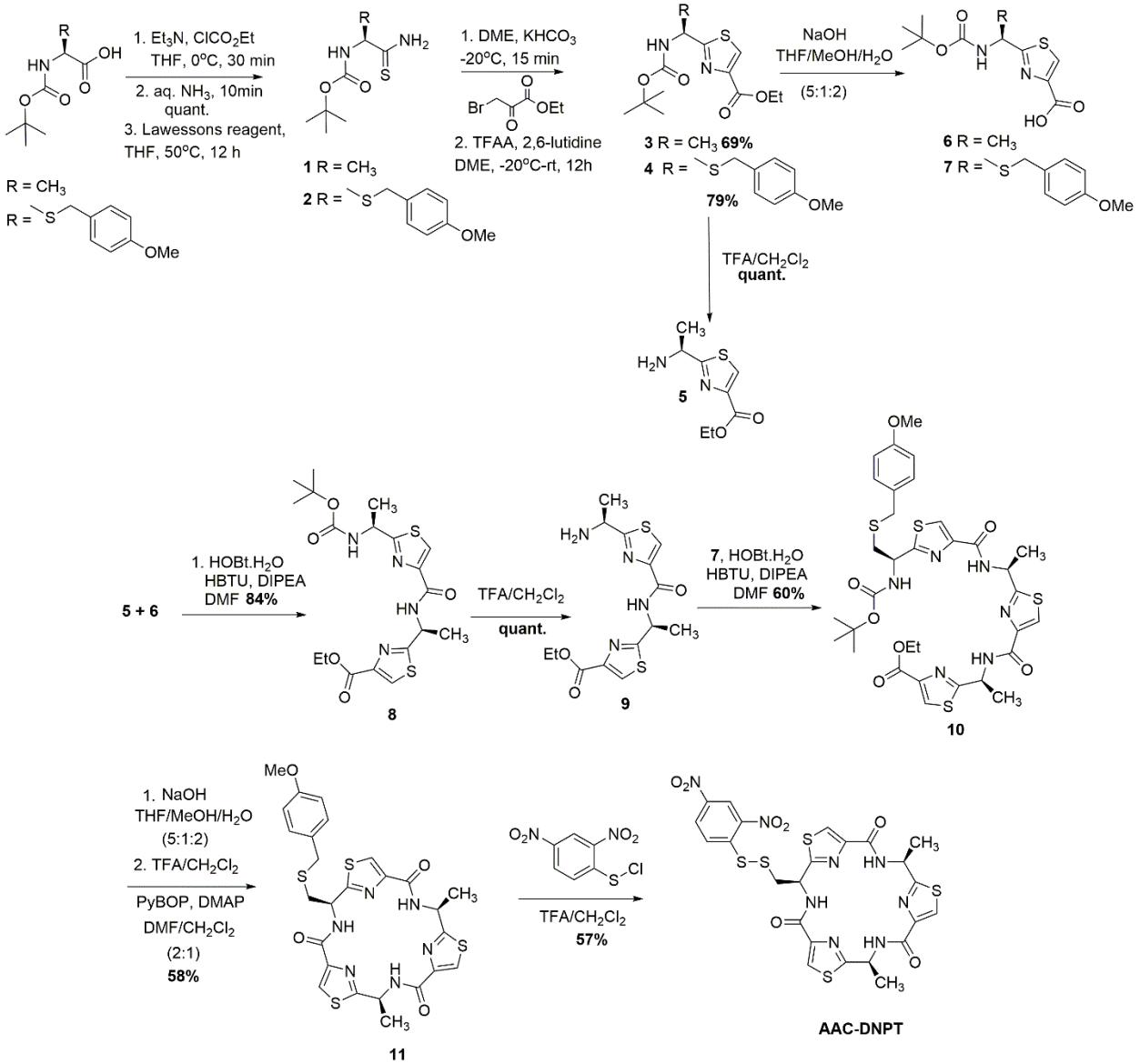

Extended Data Fig. 1. Chemical synthesis of AAC-DNPT. NMR characterization data of synthetic compounds are provided in the Supplementary Information.

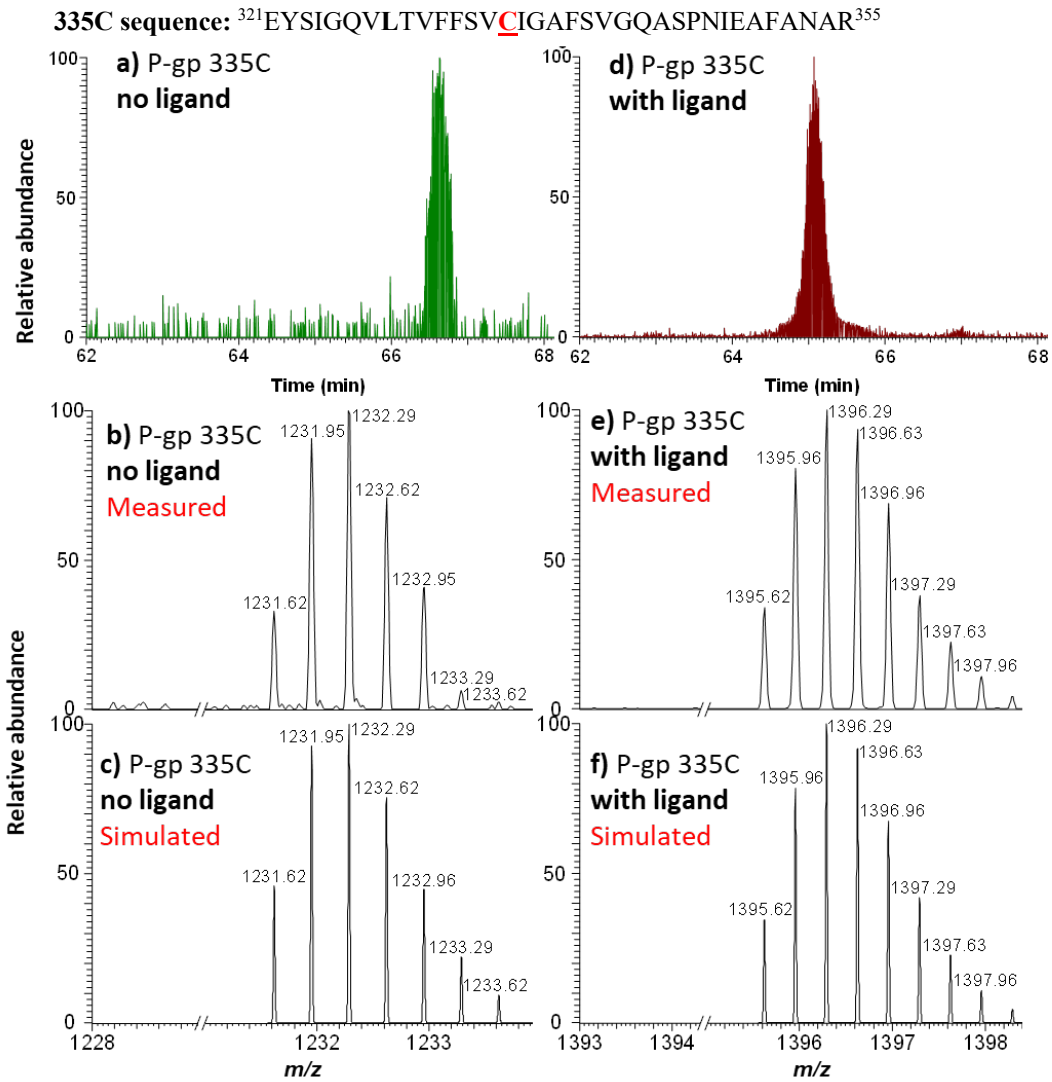

	Observed *m/z*	Theoretical *m/z*	Mass error (ppm)
335C	1232.28652	1232.28728	0.62
335C+L	1396.29317	1396.29261	0.40

Extended Data Fig. 2. MS detection of 335C peptide before and after AAC labeling. Top: 335C peptide sequence. **(a)** LC-MS trace for the 335C peptide, with **(b)** measured and **(c)** simulated m/z ($[335C+3H]^{3+}$). **(d)** LC-MS trace for the AAC-labeled 335C peptide, with **(e)** measured and **(f)** simulated m/z ($[335C+L+3H]^{3+}$). The observed isotope peak distributions for unlabeled and labeled 335C peptides are in good agreement with the simulated peak distribution; mass errors are shown in the table underneath.

978C sequence: ^{955}FGAYLVTQQLMTFENVLLVFSAICFGAMAVGQVSSFAPDYAK^{996}

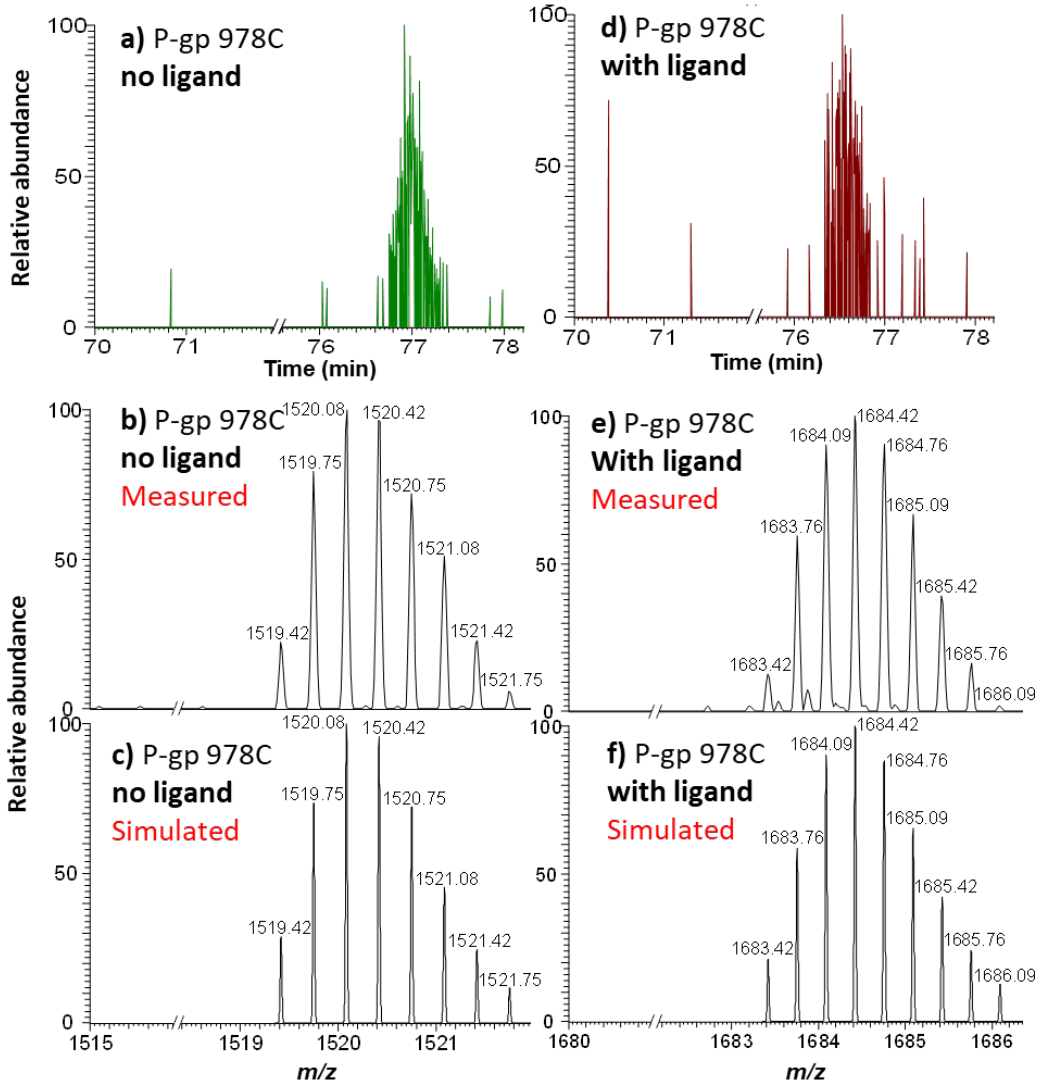

	Observed *m/z*	Theoretical *m/z*	Mass error (ppm)
978C	1520.08379	1520.08515	0.89
978C+L	1684.42427	1684.42447	0.12

Extended Data Fig. 3. MS detection of 978C peptide before and after AAC labeling. Top: 978C peptide sequence. (**a**) LC-MS trace for the 978C peptide, with (**b**) measured and (**c**) simulated m/z ([978C+2H+Na]$^{3+}$). (**d**) LC-MS trace for the AAC-labeled 978C peptide, with (**e**) measured and (**f**) simulated m/z ([978C+L+2H+Na]$^{3+}$). The observed isotope peak distributions for unlabeled and labeled 978C peptides are in good agreement with the simulated peak distributions; mass errors are shown in the table underneath.

971C sequence: ^{955}FGAYLVTQQLMTFENVCLVFSAIVFGAMAVGQVSSFAPDYAK^{996}

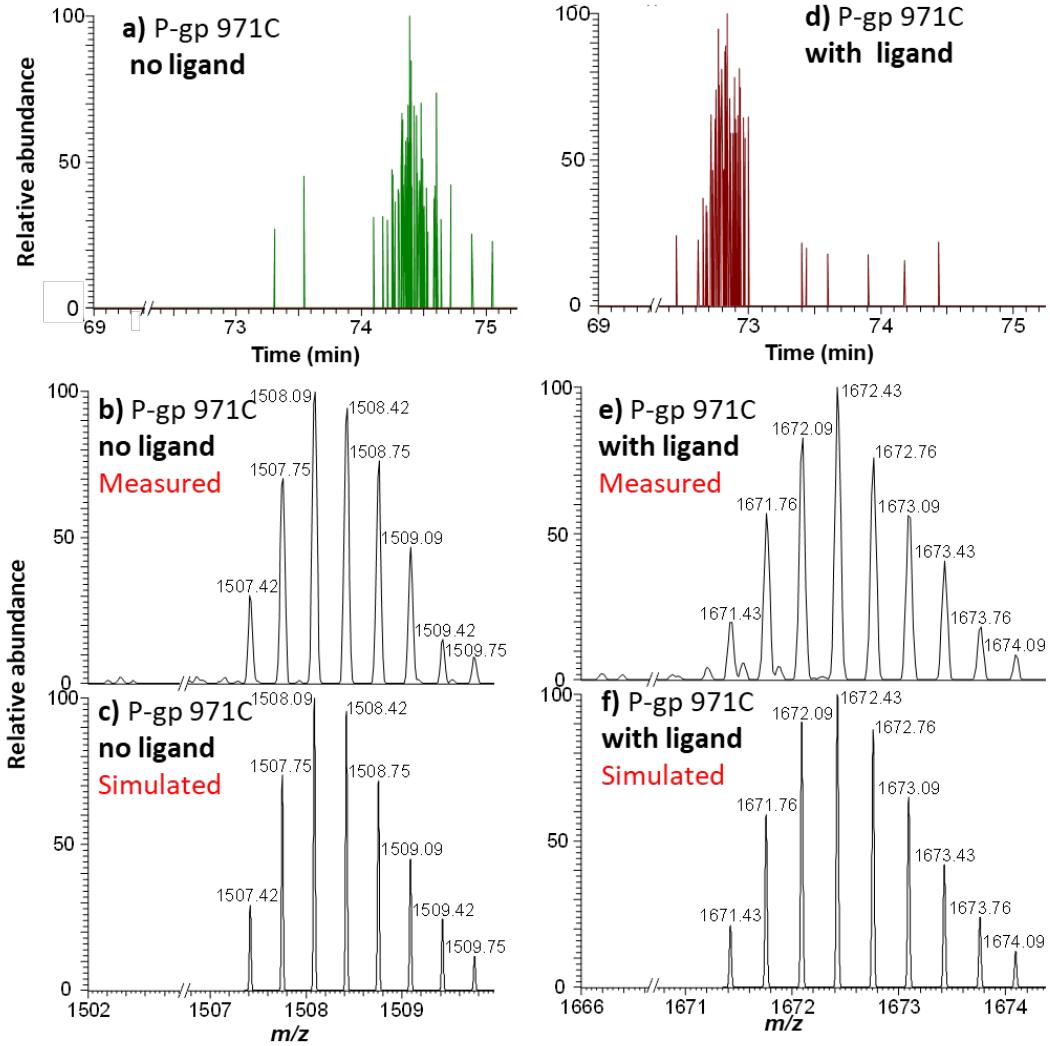

	Observed *m/z*	Theoretical *m/z*	Mass error (ppm)
971C	1508.08876	1508.08595	1.86
971C+L	1672.42763	1672.42527	1.41

Extended Data Fig. 4. MS detection of 971C peptide before and after AAC labeling. Top: 971C peptide sequence. **(a)** LC-MS trace for the 971C peptide, with **(b)** measured and **(c)** simulated m/z ($[971C+3H]^{3+}$). **(d)** LC-MS trace for the AAC-labeled 971C peptide, with **(e)** measured and **(f)** simulated m/z ($[971C+L+3H]^{3+}$). The observed isotope peak distributions for unlabeled and labeled 971C peptides are in good agreement with the simulated peak distributions; mass errors are shown in the table underneath.

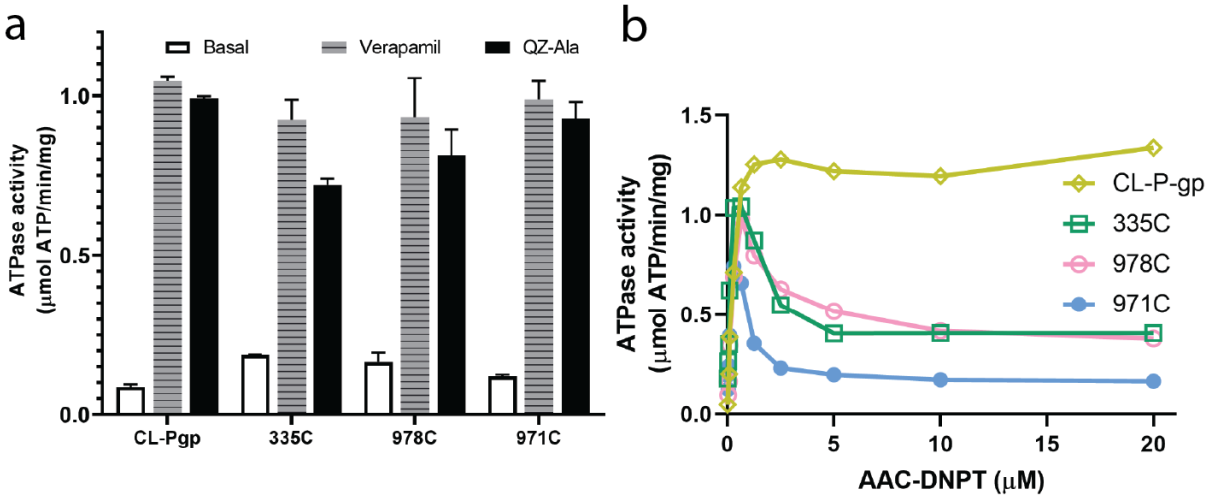

Extended Data Fig. 5. ATPase activities of Pgp mutants L335C, V978C, and L971C. (a) ATPase activity was enhanced for each mutant after addition of verapamil (30 μM) or QZ-Ala (2 μM). Data are averaged from triplicate measurements with standard error bars. **(b)** ATPase activity after addition of various concentrations of AAC-DNPT. CL-Pgp was included as control. A representative curve was shown.

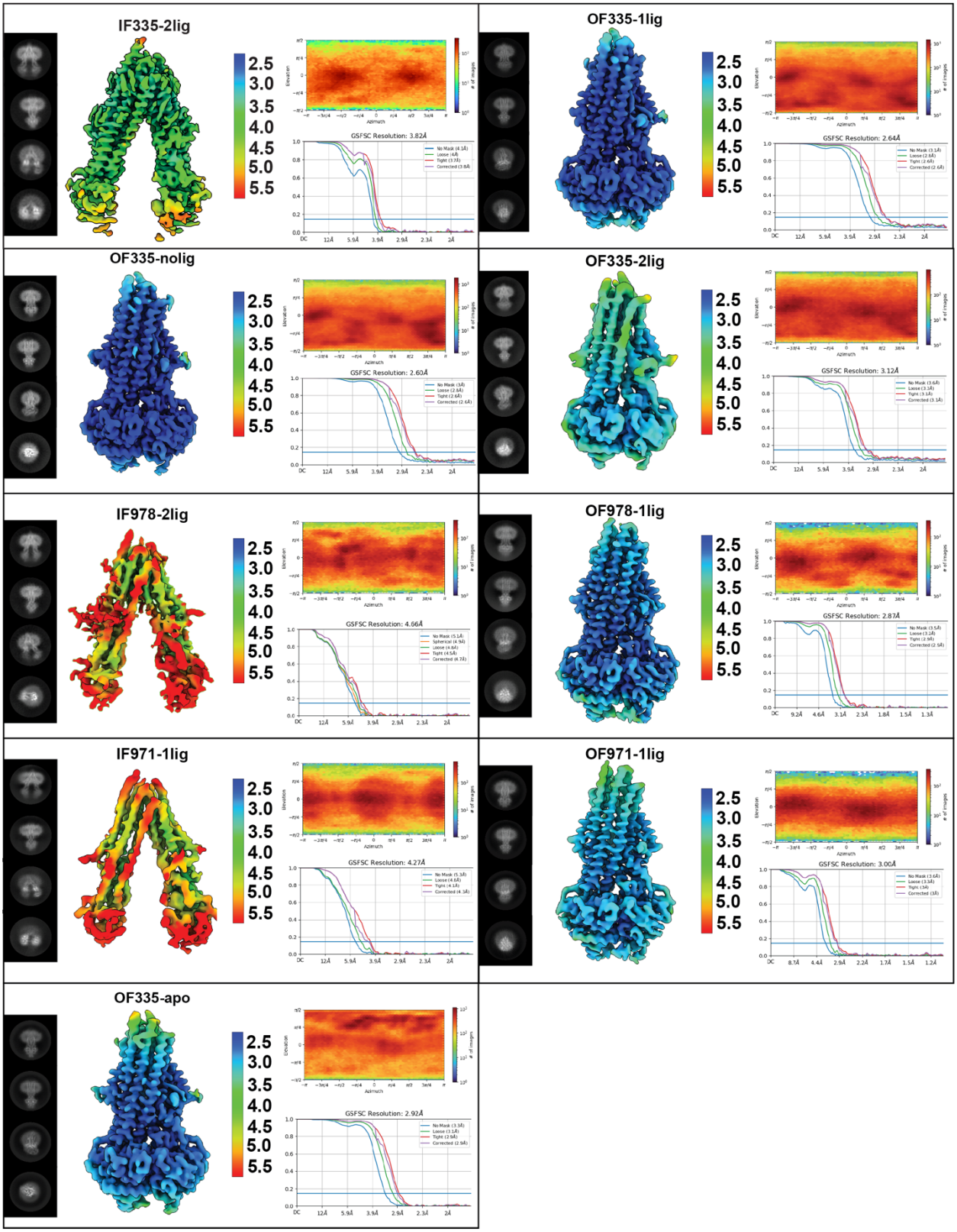
IF335-2lig
GSFSC Resolution: 3.82Å
OF335-1lig
GSFSC Resolution: 2.64Å
OF335-nolig
GSFSC Resolution: 2.60Å
OF335-2lig
GSFSC Resolution: 3.12Å
IF978-2lig
GSFSC Resolution: 4.66Å
OF978-1lig
GSFSC Resolution: 2.87Å
IF971-1lig
GSFSC Resolution: 4.27Å
OF971-1lig
GSFSC Resolution: 3.00Å
OF335-apo
GSFSC Resolution: 2.92Å
2.5
3.0
3.5
4.0
4.5
5.0
5.5

Extended Data Fig. 6. Summary of cryo-EM data analysis for all structures. Each panel shows 2D classes, local resolution estimation, viewing distribution and FSC curves for each map. All data shown here were obtained using cryoSPARC.

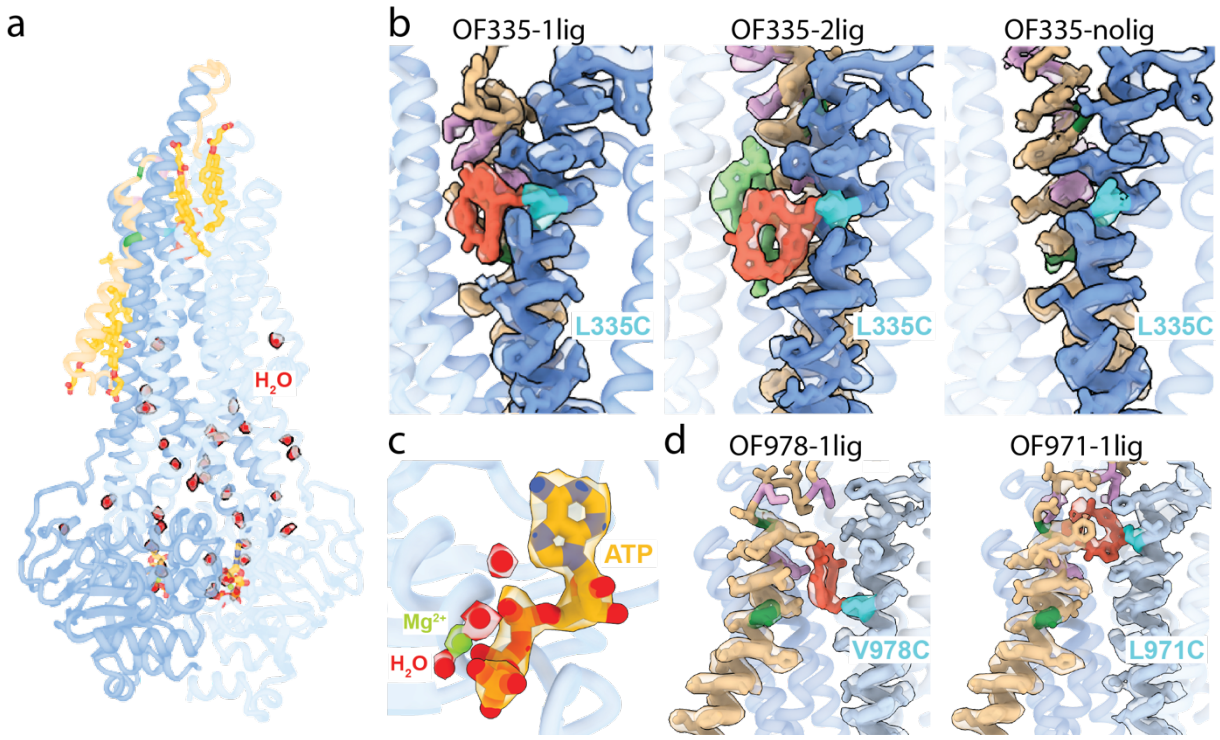

Extended Data Fig. 7. High resolution features of the OF structures. **(a)** Overall structure of OF335-1lig solved at 2.6 Å resolution. High resolution allows for fitting of water (red balls) and the surface-bound cholesterol hemisuccinate molecules (yellow sticks), in addition to the bound nucleotides and the AAC cyclopeptide. Contour level in the density modified map is 0.6. **(b)** Local densities for TM6 (blue) and TM1 (brown) in the OF Pgp335 showing the disulfide bridge in cyan between AAC (red) and TM6. AAC-DNPT is shown in light green in the OF335-2lig. Contour level used is 0.19. **(c)** Cryo-EM densities for ATP (yellow), Mg^{2+} (green) and water molecules (red) in the OF335-1lig model. Contour level in the density modified map is 0.6 (water), 1.1 (ATP) and 1.7 (Mg^{2+}). **(d)** Disulfide bridge (cyan) between TM12 (light blue) and AAC (red) for OF978-1lig and OF971-1lig. Contour levels used are 0.19 (OF978-1lig) and 0.05 (OF971-1lig). The densities for A63 and A72 (dark green) and M68,M74 and F78 (plum) are shown in each panel.

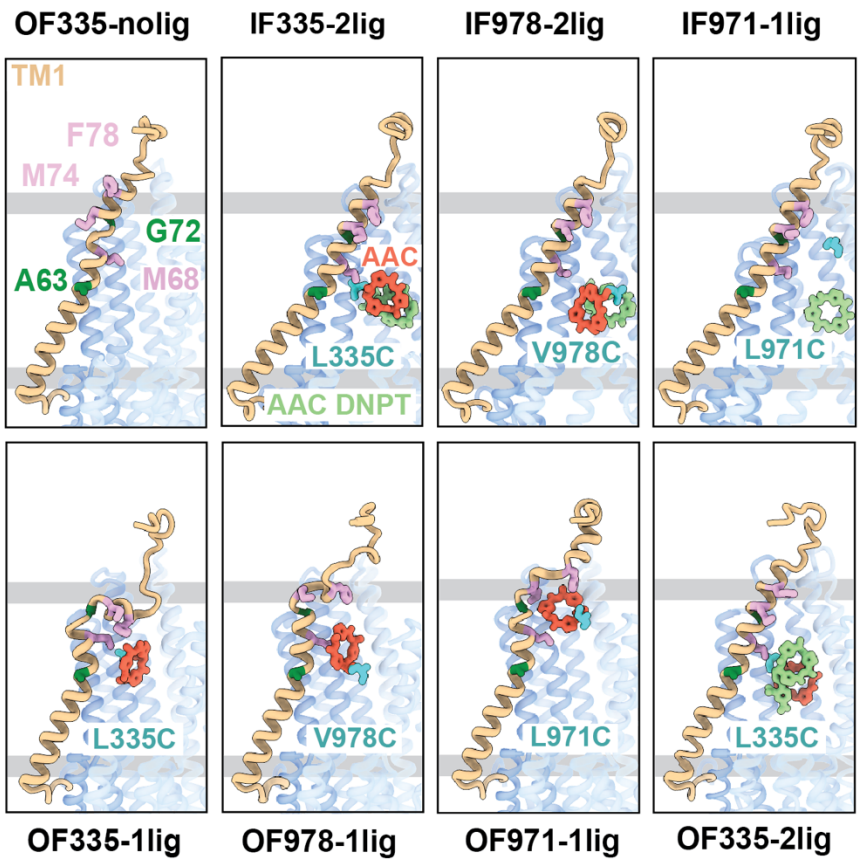

Extended Data Fig. 8. Comparison of the binding cavities of all structures from the crosslink experiments. TM1 is shown in brown, the crosslinked AAC in red and the non-crosslinked AAC-DNPT in light green, the crosslinked residue is marked in cyan. A63 and G72 are shown in dark green; M68, M75 and F78 are shown in plum.

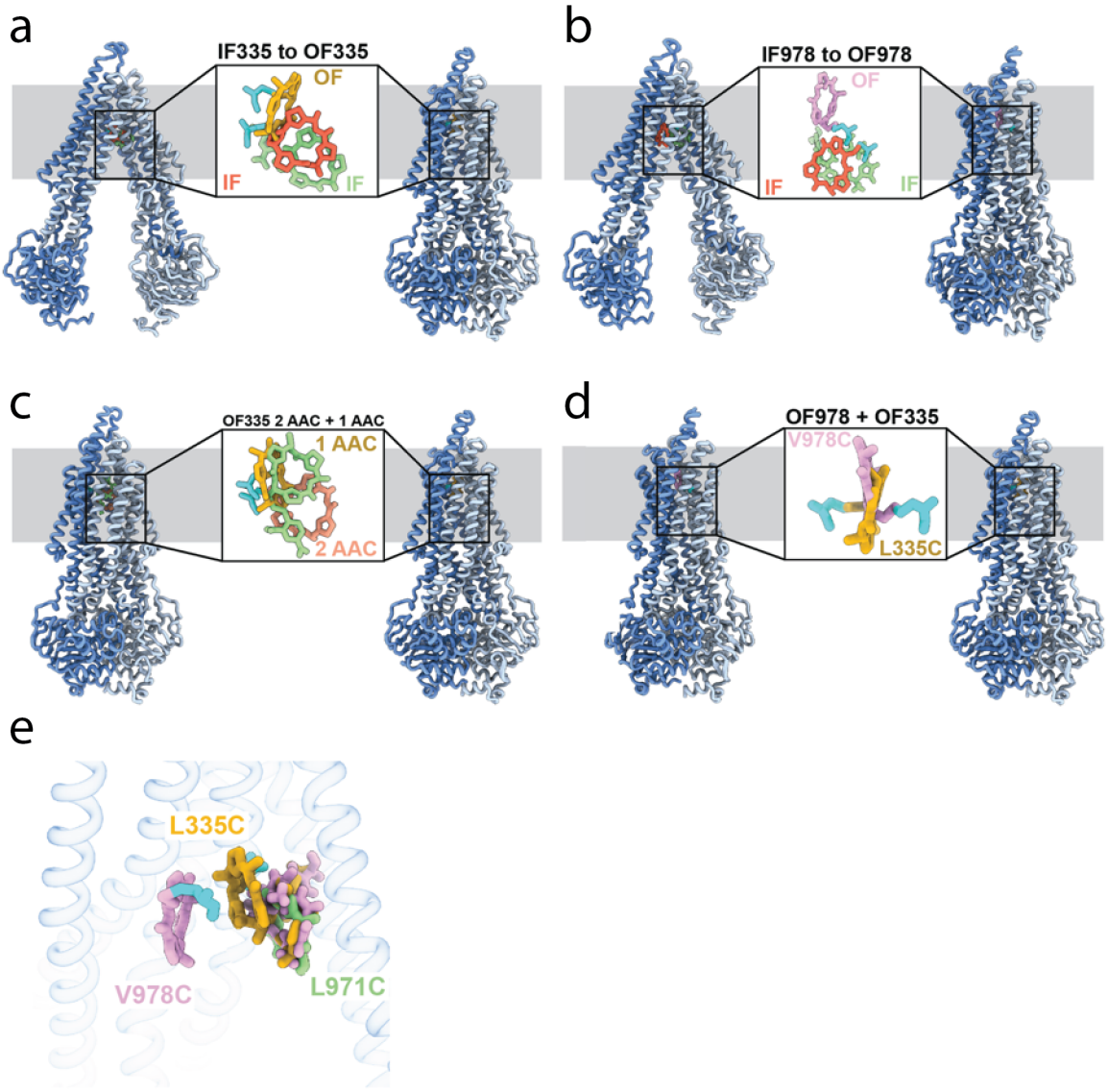

Extended Data Fig. 9. Comparison of AAC binding in the different Pgp structures. (a) Transition from IF (left) to OF (right) conformation for L335C. The IF ligand is shown in red for the crosslinked molecule, and in green for the non-crosslinked. The OF ligand is shown in yellow. **(b)** Transition from IF (left) to OF (right) for V978C. Ligand molecules for the IF conformation are shown in red (crosslinked) and green (non-crosslinked). The OF ligand is shown in plum. **(c)** Comparison between OF335 structures with 1 or 2 ligands bound. The ligands from OF335-1lig, with one molecule bound, is shown in yellow. The two molecules bound in structure OF335-2lig are shown in light pink (crosslinked) or light green (non-crosslinked). **(d)** Comparison of the ligand

position between OF335 and OF978. The ligand for OF335 is shown in yellow, for OF978 in plum. **(e)** Overlay of the ligand in the three IF structures. The ligand in IF335 is shown in yellow, in IF978 in plum, and in IF971 in light green. The crosslinked residues L335C and V978C are shown in cyan. An overall alignment in ChimeraX was used for the comparison.

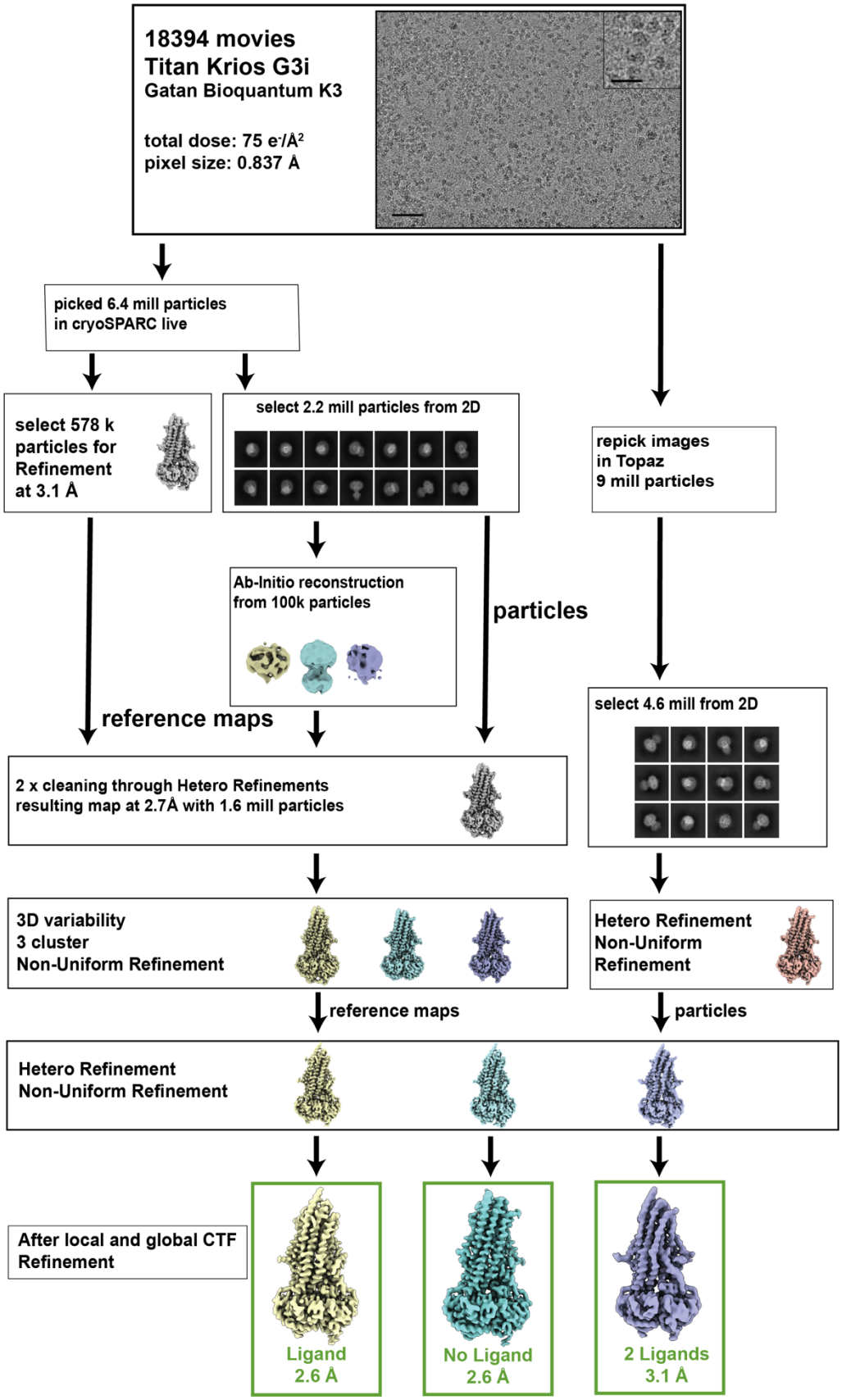
18394 movies
Titan Krios G3i
Gatan Bioquantum K3
total dose: 75 e-/Å2
pixel size: 0.837 Å
picked 6.4 mill particles
in cryoSPARC live
select 578 k
particles for
Refinement
at 3.1 Å
select 2.2 mill particles from 2D
repick images
in Topaz
9 mill particles
Ab-Initio reconstruction
from 100k particles
particles
reference maps
select 4.6 mill from 2D
2 x cleaning through Hetero Refinements
resulting map at 2.7Å with 1.6 mill particles
3D variability
3 cluster
Non-Uniform Refinement
Hetero Refinement
Non-Uniform
Refinement
reference maps
particles
Hetero Refinement
Non-Uniform Refinement
After local and global CTF
Refinement
Ligand
2.6 Å
No Ligand
2.6 Å
2 Ligands
3.1 Å

Extended Data Fig. 10. Example of cryo-EM data processing pathway for Pgp. The cryo-EM data for OF335 were collected on a Titan Krios G3i with a Gatan Bioquantum K3. In total, 18394 micrographs were collected. The entire processing pipeline was performed in cryoSPARC and cryoSPARC live. All data sets were processed in a similar manner. The scale bar is 50 nm on the micrographs and 20 nm on the inset.

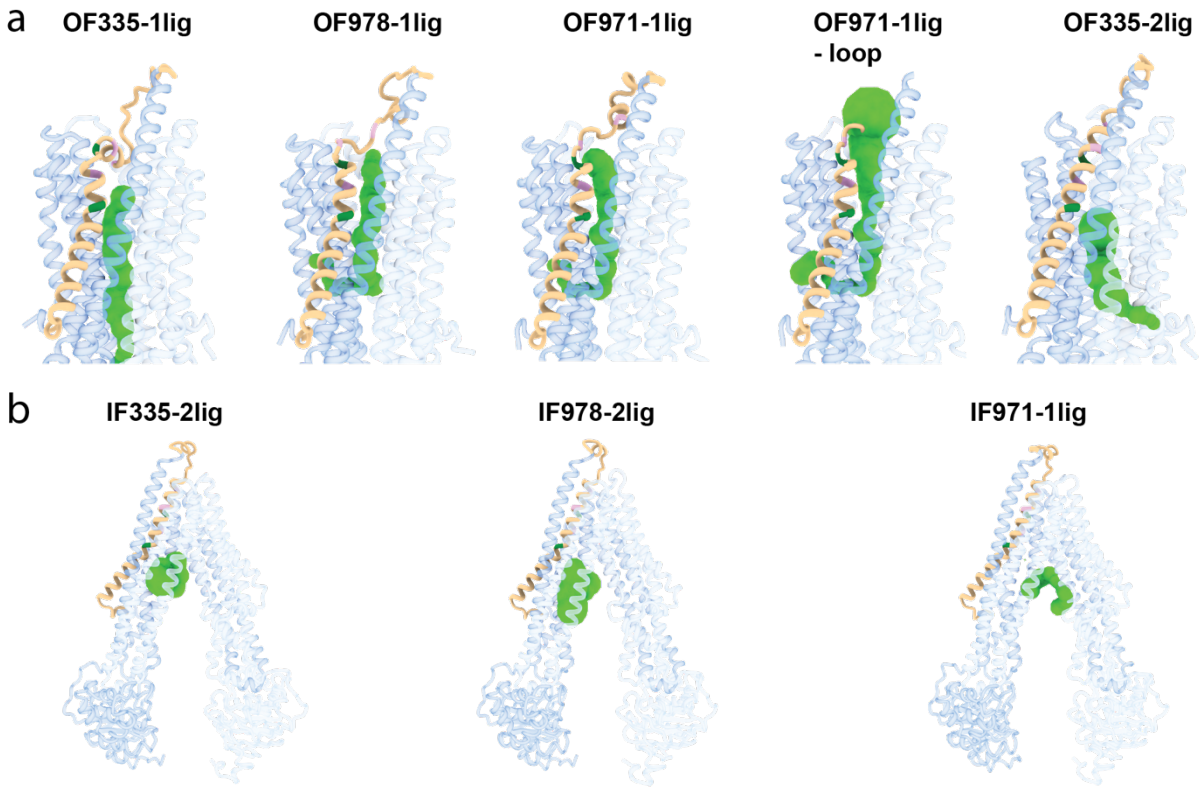

Extended Data Fig. 11. Visualization of tunnels in Pgp by the CAVER plugin for PyMOL[70]. The standard value of 3 Å was chosen as the minimum probe diameter. With OF335-nolig as template, it was not possible to calculate a tunnel. The protein is shown as cartoon and individual tunnels colored as green spheres.

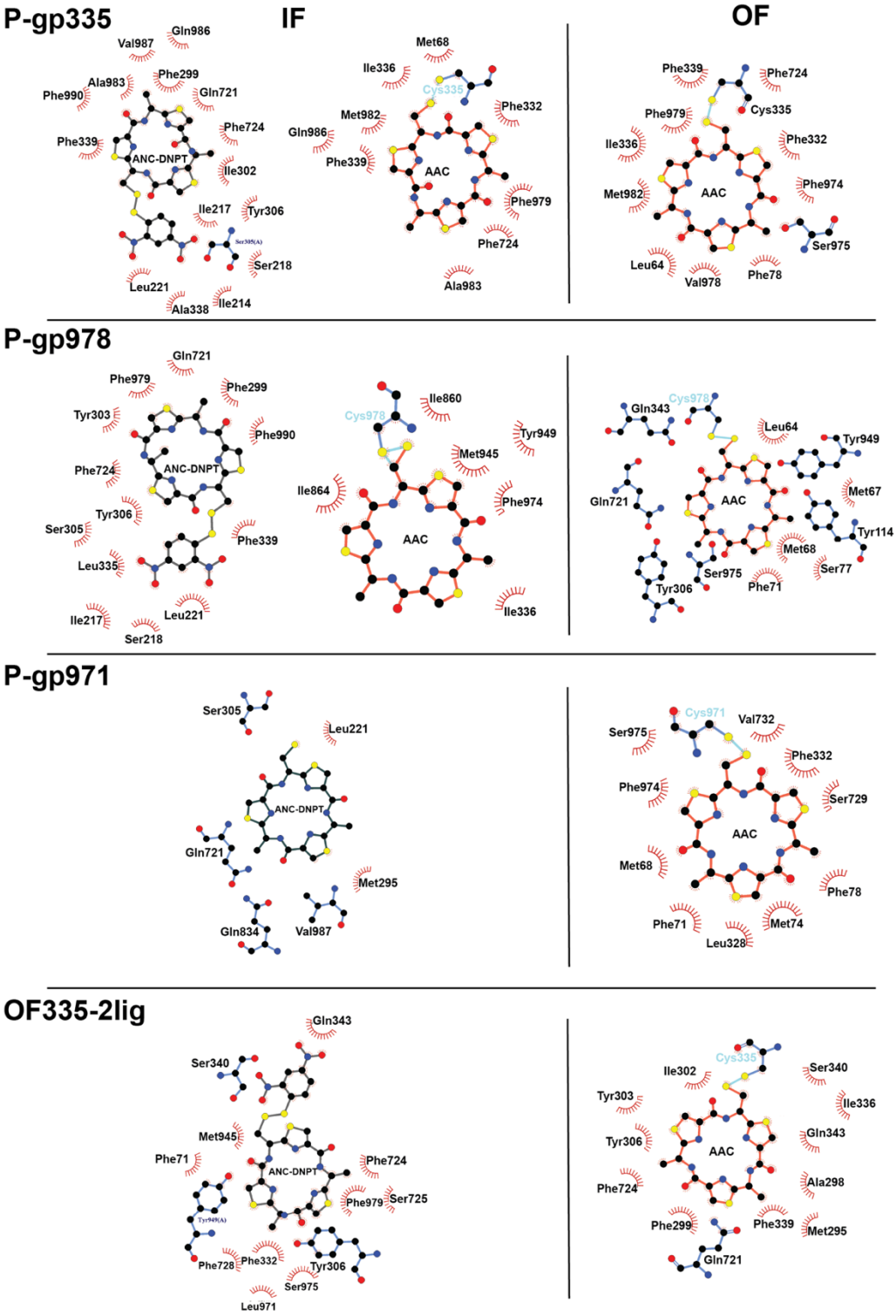

Extended Data Fig. 12. Residues in Pgp mutants interacting with AAC and AAC-DNPT. Hydrophobic interactions are shown as red halos, amino acids for hydrogen bonds are shown in

ball-and-stick representation. LigPlot+ was used for calculating and visualization of these interactions[71].

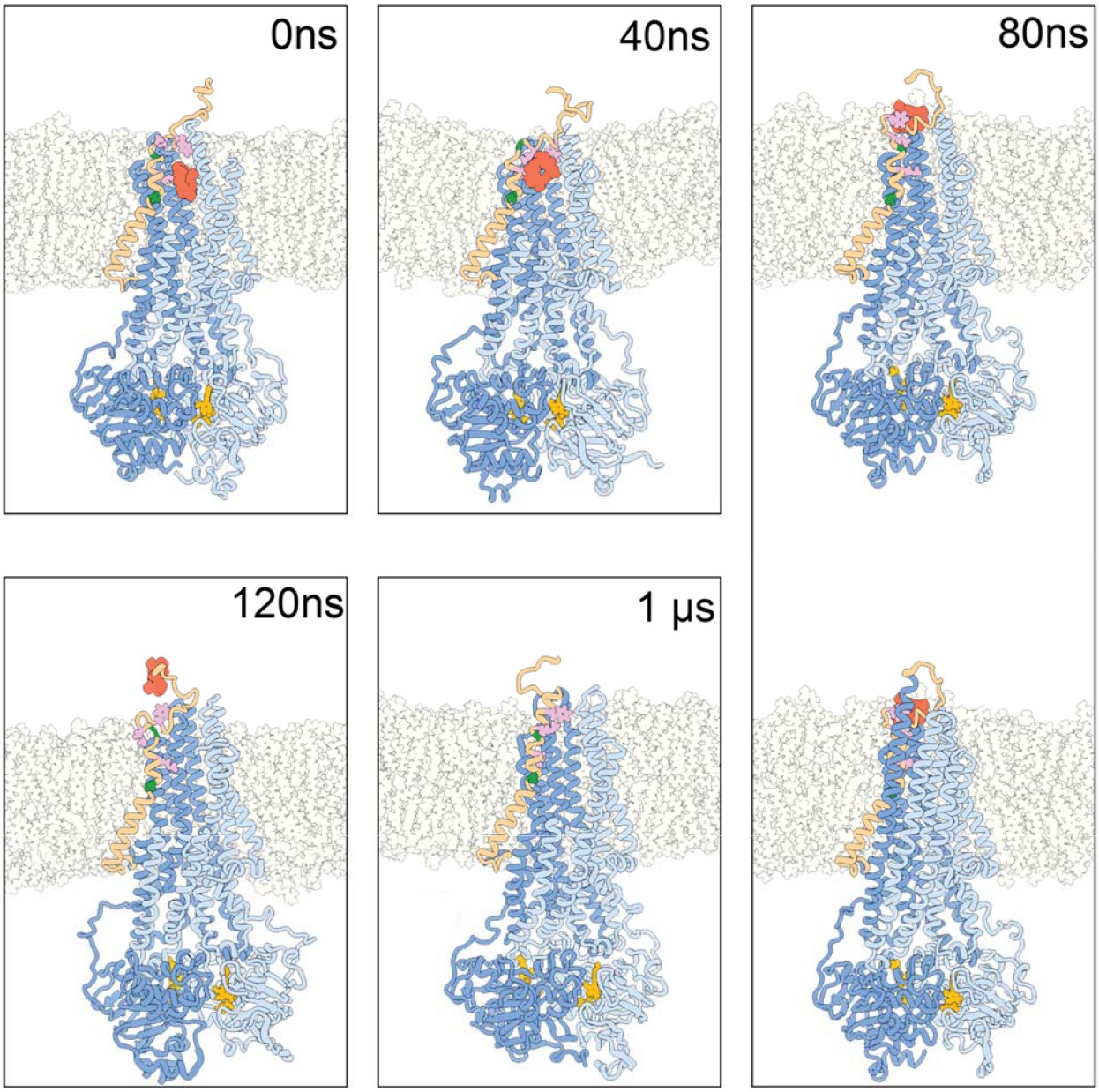

Extended Data Fig. 13. Snapshots for MD simulation started from OF978-1lig at 400K. TM1 is shown in brown, the ligand is shown in red spheres. A63 and G72 are shown in green; M68,M74 and P78 are shown in plum. The plasma membrane is shown with grey outlines. Water is not shown. **(0 ns)** Cut through the initial configuration, OF978-1lig. **(40 ns)** TM1 has rearranged while interacting with the ligand from the top. **(80 ns)** The ligand is leaving the transporter while interacting with TM1 from the side. The top panel shows a cut through the structure, the bottom

panel shows the full structure. **(120 ns)** The ligand has left the transporter and has its last transient interactions with the top of TM1. **(1us)** the end of the simulation shows a refolding of TM1.

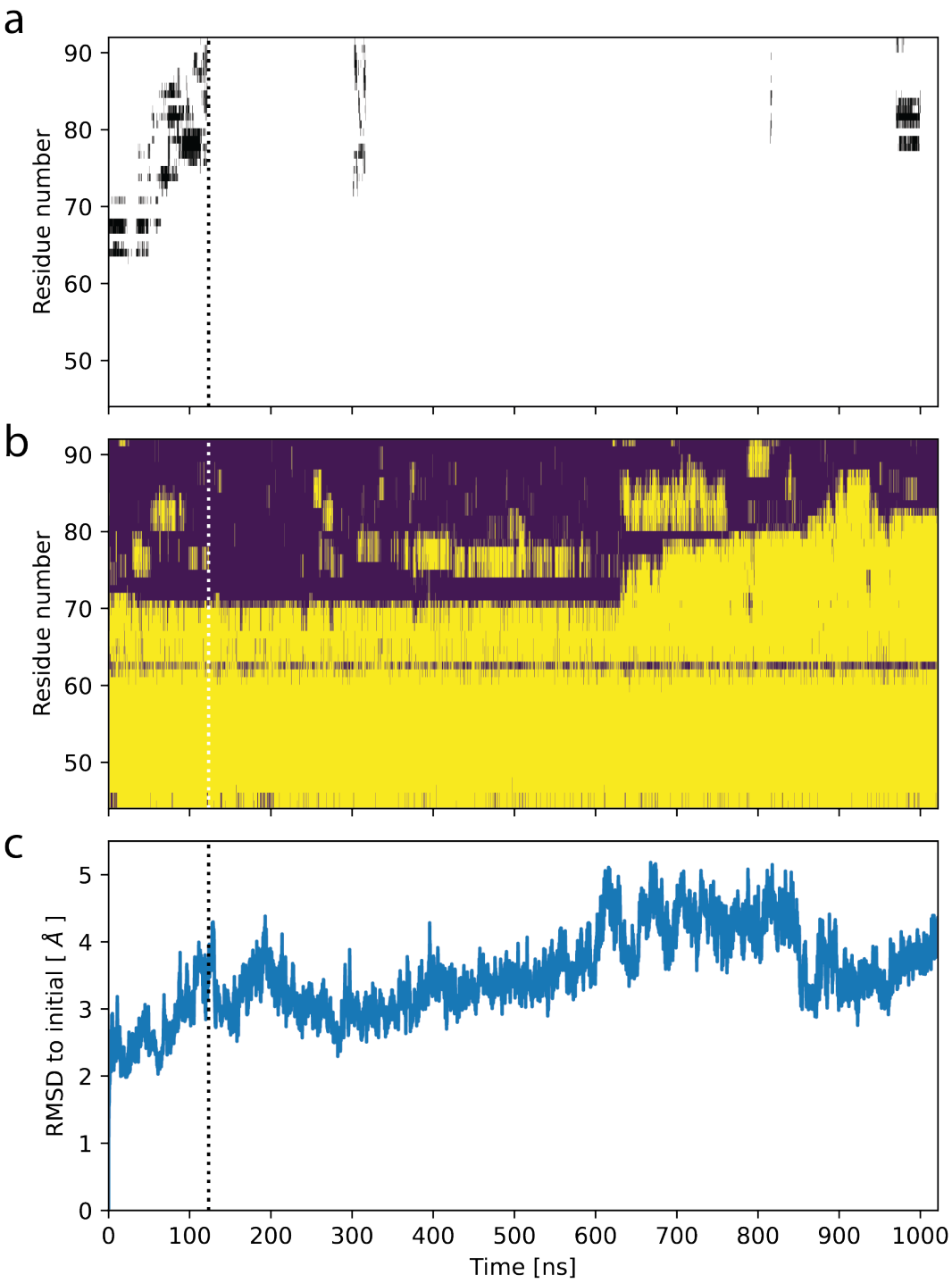

Extended Data Fig. 14. Ligand release in MD simulation starting from OF978-1lig. (a) Contacts of the ligand with residues in TM1 as function of time. Black bars indicate residues within 5 Å of the ligand. **(b)** Secondary structure in TM1 as function of time. Loop regions are shown in purple, alpha helices in yellow. **(c)** Root-mean-square distance (RMSD) of backbone atoms in Pgp

transmembrane domain (residues 34-366 and 691-1010) to initial structure as function of time. Dotted lines indicate the time point of ligand release.

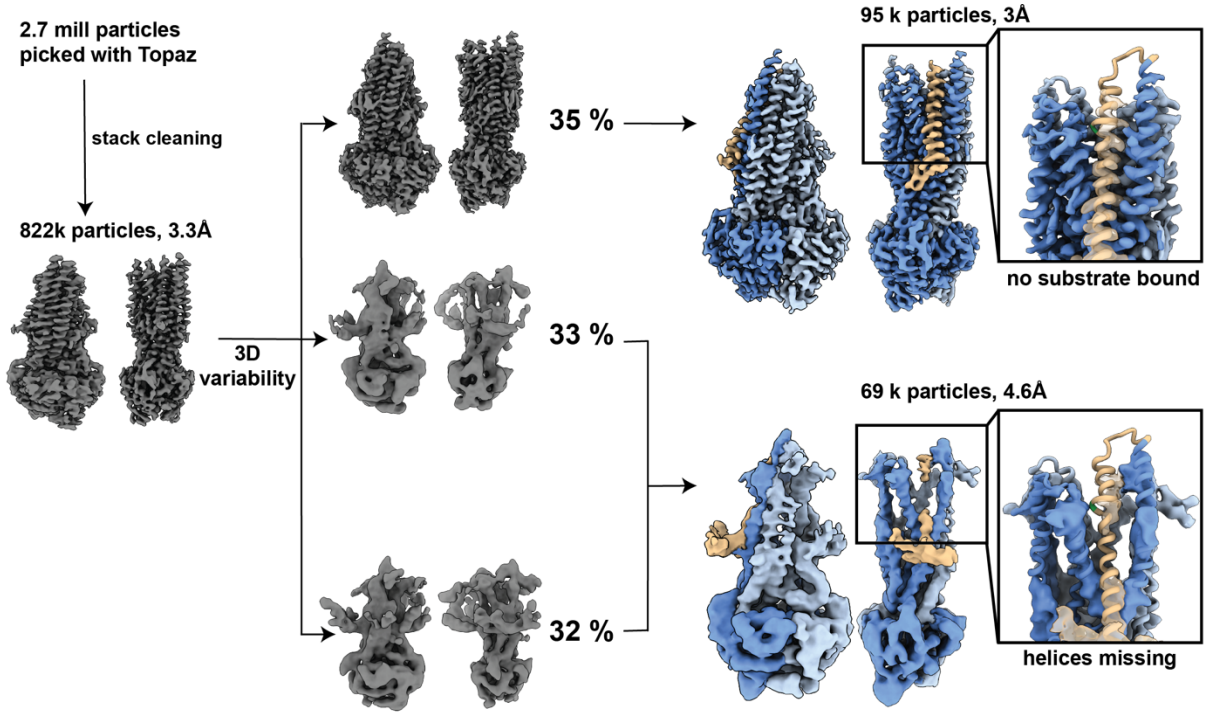

Extended Data Fig. 15: Processing overview for OF335-G72. In total, 2.7 million particles were picked using Topaz. Particle stack was cleaned through several rounds of 3D classification. Stack with 822k particles was used for 3D variability and separated into 3 clusters. Clusters were further processed with iterative rounds of 3D classifications and refinements and revealed 2 distinct conformations in the data set. An apo structure with 3Å resolution with no AAC bound and a low resolution structure of 4.6Å with poor resolution in the transmembrane helices and TM1,2,3,4,5,6,10 and 12 partially missing. Magnified images: atomic model OF335-nolig fit into the structures. TM1 is shown in brown, G72A is marked in green.

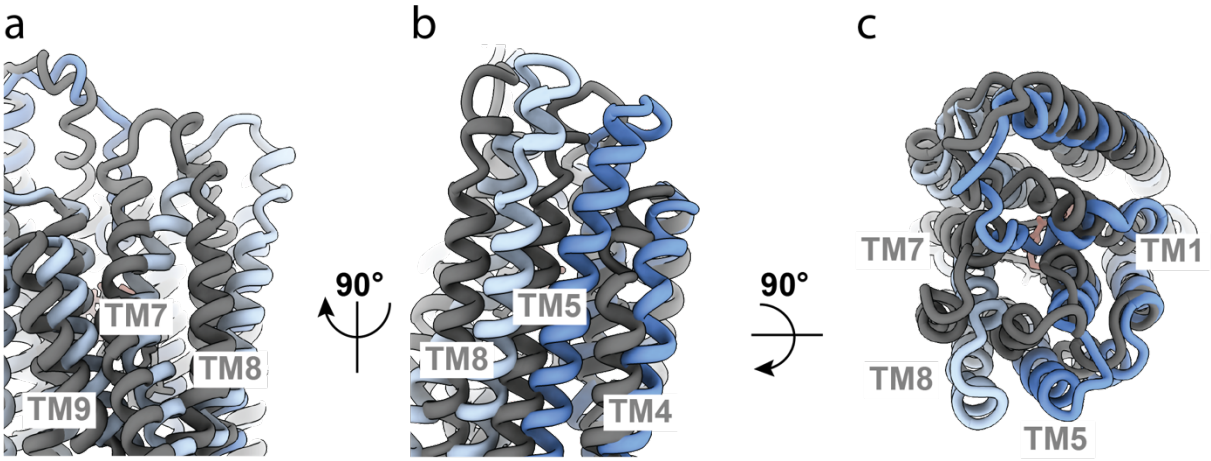

Extended Data Fig. 16. Comparison of OF335 with one AAC bound (blue) compared to two AAC molecules bound (grey). (a) Conformational differences between TM7, TM8, and TM9. The tops of helices TM7 and TM8 point in opposite directions in the two structures. **(b)** Conformational differences in TM8, TM5, and TM4. All three helices are shifted significantly with one AAC bound compared to two AAC molecules bound. **(c)** Top view comparing the two structures. The top ends of the helices are all turned further inwards when two substrate molecules are bound compared to one bound molecule. An overall alignment in ChimeraX-1.3 was used for the comparison.

Extended Data Table 1. Cryo-EM data collection, refinement, and validation statistics.

	OF335-apo (EMD-15687) (PDB 8AVY)	OF335-nolig (EMD-14754) (PDB 7ZK4)	OF335-1lig (EMD- 14755) (PDB 7ZK5)	OF335-2lig (EMD- 14756) (PDB 7ZK6)	IF335-2lig (EMD-17630) (PDB 8PEE)
Data collection					
Microscope	Titan Krios G3i	Titan Krios G3i	Titan Krios G3i	Titan Krios G3i	Titan Krios G3i
Energy filter and camera	Gatan BioQuantum K3	Gatan BioQuantum K3	Gatan BioQuantum K3	Gatan BioQuantum K3	Gatan BioQuantum K3
Energy filter slit width	30 eV	30 eV	30 eV	30 eV	30 eV
Voltage (kV)	300	300	300	300	300
Nominal magnification	105,000	105,000	105,000	105,000	105,000
Pixel size (Å)	0.837	0.837	0.837	0.837	0.837
Electron exposure ($e^-/Å^2$)	75	75	75	75	75
Total exposure time (s)	4	4	4	4	4
Number of frames per image	50	50	50	50	50
Total number of images	6594	18394	18394	18394	13999
Defocus range (μm)	-1.2 to -2.5	-1 to -2.5	-1 to -2.5	-1 to -2.5	-1 to -2.5
Image processing					
Processing software	cryoSPARC	cryoSPARC	cryoSPARC	cryoSPARC	RELION 3.1
Motion correction software	cryoSPARC	cryoSPARC	cryoSPARC	cryoSPARC	RELION3.1
CTF estimation software	cryoSPARC	cryoSPARC	cryoSPARC	cryoSPARC	Gctf
Particle selection software	Topaz	Topaz	Topaz	Topaz	RELION 3.1
Initial particle images (no.)	2,262,305	9,065,013	9,065,013	9,065,013	2,975,426
Final particle images (no.)	790,159	1,437,110	1,184,253	939,924	218,872
Final refinement software	cryoSPARC	cryoSPARC	cryoSPARC	cryoSPARC	cryoSPARC
Symmetry imposed	C1	C1	C1	C1	C1
Map resolution (Å)	2.9	2.6	2.6	3.1	3.8
B-factor ($Å^2$)	138.2	119.3	118.6	154.8	155.2
Refinement statistics					
Initial model (PDB code)	6C0V	6C0V	6C0V	6C0V	4Q9I
Modeling software	Coot, PHENIX	Coot, PHENIX	Coot, PHENIX	Coot, PHENIX	Coot, PHENIX
Model composition					
Non-hydrogen atoms	9433	9371	9436	9267	9217
Protein residues	1175	1176	1177	1177	1157
Water molecules	4	4	33	4	-
Ligands	12	9	10	7	7
Mean *B* factors ($Å^2$)					
Protein	27.15	27	39	59	71
Water molecules	-	-	37	30	-
Ligand	37.03	59	44	50	57
R.m.s. deviations					
Bond lengths (Å)	0.030	0.024	0.024	0.019	0.024
Bond angles (°)	1.265	1.04	1.16	0.91	1.040
Validation					
MolProbity score	1.50	1.50	1.56	1.49	2.00
Clashscore	9.39	9.29	9.43	9.33	12.52
Poor rotamers (%)	0.74	0.10	0.10	0.10	0.32

Ramachandran plot					
Favored (%)	98.04	97.95	97.70	98.12	94.19
Allowed (%)	1.96	2.05	2.22	1.79	5.81
Disallowed (%)	0.00	0.00	0.08	0.09	0.00

	OF971-1lig (EMD- 14758) (PDB 7ZK8)	IF971-1lig (EMD- 14759) (PDB 7ZK9)	OF978-1lig (EMD- 14760) (PDB 7ZKA)	IF978-2lig (EMD- 14761) (PDB 7ZKB)
Data collection				
Microscope	Titan Krios G4	Titan Krios G3i	Titan Krios G4	Titan Krios G3i
Energy filter and camera	Selectris X Falcon 4	Gatan BioQuantum K3	Selectris X Falcon 4	Gatan BioQuantum K3
Energy filter slit width	10 eV	30 eV	10 eV	30 eV
Voltage (kV)	300	300	300	300
Nominal magnification	215,000	105,000	215,000	105,000
Pixel size (Å)	0.537	0.837	0.537	0.837
Electron exposure ($e^-/Å^2$)	70	75	70	75
Total exposure time (s)	4	4	4	4
Number of frames per image	70	50	70	50
Total number of images	12128	6758	14998	6204
Defocus range (μm)	-1 to -2.5	-1 to -2.5	-1 to -2.5	-1 to -2.5
Image processing				
Processing software	cryoSPARC	cryoSPARC	cryoSPARC	cryoSPARC
Motion correction software	cryoSPARC	cryoSPARC	cryoSPARC	cryoSPARC
CTF estimation software	cryoSPARC	cryoSPARC	cryoSPARC	cryoSPARC
Particle selection software	Topaz	cryoSPARC	cryoSPARC	cryoSPARC
Initial particle images (no.)	1,644,112	1,664,538	1,761,489	1,744,204
Final particle images (no.)	298,192	443,812	271,467	343,873
Final refinement software	CryoSPARC	CryoSPARC	CryoSPARC	CryoSPARC
Symmetry imposed	C1	C1	C1	C1
Map resolution (Å)	3.0	4.3	2.9	4.7
B-factor ($Å^2$)	128.1	285	116.8	347.4
Refinement statistics				
Initial model (PDB code)	6C0V	4Q9I	6C0V	4Q9I
Modeling software	Coot, PHENIX	Coot, PHENIX	Coot, PHENIX	Coot, PHENIX
Model composition				
Non-hydrogen atoms	9331	9004	9407	9035
Protein residues	1181	1157	1177	1157
Water molecules	4	-	4	-
Ligands	7	1	9	2
Mean *B* factors ($Å^2$)				
Protein	56	181	31	121
Water molecules	33	-	12	-
Ligand	55	154	37	71
R.m.s. deviations				
Bond lengths (Å)	0.016	0.005	0.003	0.004
Bond angles (°)	1.00	0.92	0.59	0.80
Validation				
MolProbity score	1.74	2.07	1.69	2.08
Clashscore	9.69	15.76	9.86	13.26
Poor rotamers (%)	0.10	0.21	0.00	0.00
Ramachandran plot				
Favored (%)	96.52	94.62	97.02	93.06

Allowed (%)	3.48	5.29	2.90	6.94
Disallowed (%)	0.00	0.09	0.08	0.00

	OF971-1lig (EMD- 14758) (PDB 7ZK8)	IF971-1lig (EMD- 14759) (PDB 7ZK9)	OF978-1lig (EMD- 14760) (PDB 7ZKA)	IF978-2lig (EMD- 14761) (PDB 7ZKB)
Data collection				
Microscope	Titan Krios G4	Titan Krios G3i	Titan Krios G4	Titan Krios G3i
Energy filter and camera	Selectris X Falcon 4	Gatan BioQuantum K3	Selectris X Falcon 4	Gatan BioQuantum K3
Energy filter slit width	10 eV	30 eV	10 eV	30 eV
Voltage (kV)	300	300	300	300
Nominal magnification	215,000	105,000	215,000	105,000
Pixel size (Å)	0.537	0.837	0.537	0.837
Electron exposure (e^-/Å^2)	70	75	70	75
Total exposure time (s)	4	4	4	4
Number of frames per image	70	50	70	50
Total number of images	12128	6758	14998	6204
Defocus range (µm)	-1 to -2.5	-1 to -2.5	-1 to -2.5	-1 to -2.5
Image processing				
Processing software	cryoSPARC	cryoSPARC	cryoSPARC	cryoSPARC
Motion correction software	cryoSPARC	cryoSPARC	cryoSPARC	cryoSPARC
CTF estimation software	cryoSPARC	cryoSPARC	cryoSPARC	cryoSPARC
Particle selection software	Topaz	cryoSPARC	cryoSPARC	cryoSPARC
Initial particle images (no.)	1,644,112	1,664,538	1,761,489	1,744,204
Final particle images (no.)	298,192	443,812	271,467	343,873
Final refinement software	CryoSPARC	CryoSPARC	CryoSPARC	CryoSPARC
Symmetry imposed	C1	C1	C1	C1
Map resolution (Å)	3.0	4.3	2.9	4.7
B-factor (Å^2)	128.1	285	116.8	347.4
Refinement statistics				
Initial model (PDB code)	6C0V	4Q9I	6C0V	4Q9I
Modeling software	Coot, PHENIX	Coot, PHENIX	Coot, PHENIX	Coot, PHENIX
Model composition				
Non-hydrogen atoms	9331	9004	9407	9035
Protein residues	1181	1157	1177	1157
Water molecules	4	-	4	-
Ligands	7	1	9	2
Mean *B* factors (Å^2)				
Protein	56	181	31	121
Water molecules	33	-	12	-
Ligand	55	154	37	71
R.m.s. deviations				
Bond lengths (Å)	0.016	0.005	0.003	0.004
Bond angles (°)	1.00	0.92	0.59	0.80
Validation				
MolProbity score	1.74	2.07	1.69	2.08
Clashscore	9.69	15.76	9.86	13.26
Poor rotamers (%)	0.10	0.21	0.00	0.00
Ramachandran plot				
Favored (%)	96.52	94.62	97.02	93.06
Allowed (%)	3.48	5.29	2.90	6.94
Disallowed (%)	0.00	0.09	0.08	0.00

Extended Data Table 2: Equilibration protocol for MD simulations.

Equilibration step	Time $[ps]$	Timestep $[ps]$	Ensemble	Thermostat	Barostat	Force constant backbone $\left[\frac{kJ}{molnm^2}\right]$	Force constant side chain $\left[\frac{kJ}{molnm^2}\right]$	Force constant lipids $\left[\frac{kJ}{molnm^2}\right]$	Force constant dihedrals $\left[\frac{kJ}{molrad^2}\right]$
1	125	0.001	NVT	Berendsen		4000	2000	1000	1000
2	125	0.001	NVT	Berendsen		2000	1000	400	400
3	125	0.001	NPT	Berendsen	Berendsen (semi-isotropic)	1000	500	400	200
4	500	0.002	NPT	Berendsen	Berendsen (semi-isotropic)	500	200	200	200
5	500	0.002	NPT	Berendsen	Berendsen (semi-isotropic)	200	50	40	100
6	500	0.002	NPT	Berendsen	Berendsen (semi-isotropic)	50	0	0	0